JGR Earth Surface

RESEARCH ARTICLE
10.1029/2024JF007792

Waterfalls Alter Reach-Scale Fluvial Erosion Rates: Evidence From Field Data and Process Modeling

Sophie D. Rothman[1], **Joel S. Scheingross**[2], **and Scott W. McCoy**[2]

[1]Graduate Program of Hydrologic Science, University of Nevada, Reno, Reno, NV, USA, [2]Nevada Geosciences, Department of Geologic Science and Engineering, University of Nevada, Reno, Reno, NV, USA

Key Points:

- Cosmogenic analysis indicates that the waterfall-rich study reaches erode at or above the basin averaged erosion rate
- Waterfall frequency is the strongest indicator of reach-averaged erosion rate in waterfall-rich study reaches
- Model results suggest that waterfall-rich reaches may erode slower than waterfall-free reaches under high sediment loads

Supporting Information:

Supporting Information may be found in the online version of this article.

Correspondence to:

S. D. Rothman,
srothman@unr.edu

Citation:

Rothman, S. D., Scheingross, J. S., & McCoy, S. W. (2024). Waterfalls alter reach-scale fluvial erosion rates: Evidence from field data and process modeling. *Journal of Geophysical Research: Earth Surface*, *129*, e2024JF007792. https://doi.org/10.1029/2024JF007792

Received 20 APR 2024
Accepted 4 DEC 2024
Corrected 6 JAN 2025

This article was corrected on 6 JAN 2025. See the end of the full text for details.

Abstract Waterfalls are often interpreted as transient, upstream-propagating features that mark changes in external conditions. Thus, waterfalls are commonly used to infer past tectonic and climatic forcing, making understanding the controls on waterfall erosion central to predicting how external perturbations move through landscapes. Surprisingly, there exist few direct field measurements of waterfall erosion, and existing waterfall retreat measurements are rarely paired with measurements of waterfall morphology and frequency, which, theory suggests, modulate retreat rates. This lack of data limits our ability to test existing theory and explore how waterfalls alter reach-scale bedrock erosion rates. Here, we use cosmogenic ^{10}Be accumulated in bedrock riverbeds to measure erosion rates in fluvial reaches with varying waterfall frequency and morphology. We find that waterfall-rich reaches erode one to five times faster than the landscape average, and that reach-averaged erosion rates increase with increasing waterfall frequency. We develop a new, process-based model combining waterfall and planar-channel erosion to explore mechanistic controls on the relative erosion rate between waterfall-rich and waterfall-free reaches. This model predicts that reach-averaged erosion rates increase with waterfall frequency at low sediment supply, consistent with our field measurements, but that waterfalls can also slow reach-averaged erosion rates for high sediment supply, large grain sizes, low water discharge, or large plunge pools. Our work is consistent with previous suggestions that waterfall erosion rates may decrease in low drainage areas and can influence long-profile morphology.

Plain Language Summary Waterfalls are often created by geologic or climatic events (e.g., changes in fault motion or sea level), allowing scientists to learn about geologic history from waterfall erosion and retreat. While previous studies show how fast waterfalls or sections of rivers (reaches) with waterfalls move upstream, few studies have examined how waterfall retreat rate is affected by waterfall geometry and frequency. Here, we studied ten waterfall-rich reaches in the Kings and Kaweah Rivers in the southern Sierra Nevada, CA. We used geochemical measurements of river bedrock and sand to assess the long-term erosion rate of the reaches and surrounding landscapes. We found that all 10 reaches eroded at or above the average landscape erosion rate and that waterfall frequency was the best indicator of reach erosion rate. We then created a model of how rivers erode through mixed waterfall and non-waterfall processes. We used the model to examine how fast waterfall-rich reaches erode under a range of conditions and found that sometimes, especially under large and abundant sediment loads, waterfalls can slow erosion. These findings increase our understanding of how river erosion and river form can differ from place to place.

1. Introduction

Bedrock rivers are crucial for interpreting landscape history. Bedrock rivers transmit climatic and tectonic perturbations through basins and can record these perturbations via km-scale reaches with elevated slope (which we define as knickzones), which often contain a series of waterfalls (defined by the detachment of water from the waterfall face) (Beeson & McCoy, 2019; Berlin & Anderson, 2007; Brocard et al., 2016; Crosby & Whipple, 2006; DiBiase et al., 2015). In some cases, waterfalls can form by external base-level forcing, for example, via accumulation of fault slip (Malatesta & Lamb, 2018; Yanites et al., 2010) or cliff erosion following sea-level change (Mackey et al., 2014). In other cases, steepening of river channels caused by changes in base level or otherwise can trigger morphodynamic instabilities in the form of small repeating bedrock steps, called cyclic steps, which can grow into waterfalls, illustrating waterfall self-formation as a bedrock bedform (Baynes, Lague, & Kermarrec, 2018; Groh & Scheingross, 2022; Izumi et al., 2017; Scheingross et al., 2019, 2020). Independent of whether waterfalls form due to internal or external forcing, all waterfalls have a free-falling waterfall jet, and commonly have plunge pools that the jet and entrained sediment have eroded and shaped (Figure S1 in Supporting

Information S1) (Gilbert, 1890; Howard et al., 1994; Lamb et al., 2007). Interpreting how landscapes with waterfalls respond to external forcing, thus requiring an understanding of the controls on waterfall plunge-pool erosion and waterfall-channel interactions. For example, waterfalls that erode fast or slow relative to a waterfall-free channel may result in km-scale changes in river long profile morphology that can potentially obscure standard expectations for river long profile morphology following base level change (DiBiase et al., 2015; Rothman et al., 2023; Scheingross et al., 2020).

Despite the importance of waterfall retreat rate for landscape evolution studies, existing theory, flume, and field data do not provide a clear picture of when and why reaches with waterfalls will erode faster or slower than similar, waterfall-free river reaches (cases that we term "fast waterfalls" and "slow waterfalls,' respectively). Field measurements and remotely sensed data suggest that waterfalls erode fast in areas with high drainage area, and slow near the headwaters, where transport stage drops due to increasing sediment size, and decreasing water discharge (Berlin & Anderson, 2007; Crosby & Whipple, 2006; DiBiase et al., 2015; Raming et al., 2024; Raming & Whipple, 2022). However, these studies do not account for the fact that retreat rate can also be influenced by differences in waterfall morphology and erosion mechanisms (e.g., Lamb & Dietrich, 2009; Scheingross & Lamb, 2017). Furthermore, the idea that waterfall retreat rate scales with drainage area is not universal, and multiple studies have shown waterfall retreat rates that are independent of drainage area (Baynes, Lague, Attal, et al., 2018; Mackey et al., 2014). Existing physics-based theory provides a framework to assess erosion rates at individual waterfalls (Lamb & Dietrich, 2009; Scheingross & Lamb, 2017) and in planar bedrock channels (Lamb et al., 2008; Sklar & Dietrich, 2001; Zhang et al., 2015) that can be used to predict if waterfall erosion is fast or slow relative to waterfall-free reaches. However, these models commonly assume specific processes (e.g., waterfall retreat via toppling of bedrock columns (Lamb & Dietrich, 2009) or via vertical plunge pool drilling (Scheingross & Lamb, 2017)), which may not be present at every waterfall. Furthermore, the processes included in the existing theory may not control the speed of waterfall retreat. For example, recent experimental work (Inoue et al., 2023) suggests that, for short drop heights, the rate of formation of new bedrock cyclic steps upstream of a waterfall, which may erode into new waterfalls, is an important component of waterfall retreat; however, this new-step-formation rate is not included in existing waterfall retreat theory.

Arguably, the most robust way to assess waterfall erosion rate is via direct field measurements. A robust field-assessment, examining if waterfalls accelerate or slow reach-scale erosion rates, requires measuring multiple waterfall erosion rates across a field area while systematically varying key variables thought to control the relative erosion rate (e.g., waterfall morphology, waterfall frequency, sediment supply, and more). However, such data are extremely limited. Existing studies tend to focus on retreat of knickzones without documenting or explicitly exploring the role of waterfall geometry, waterfall frequency, or other waterfall features that may be key to setting retreat rates (e.g., Brocard et al., 2016; Crosby & Whipple, 2006; DiBiase et al., 2015; Jansen et al., 2011; Perron & Royden, 2013; Roda-Boluda et al., 2019; Whittaker & Boulton, 2012). In cases explicitly documenting waterfall retreat, studies often focus on a single waterfall (e.g., Baynes et al., 2015; Gilbert, 1907; Mackey et al., 2014; Valla et al., 2010), limiting our ability to link differences in morphology between waterfalls to retreat rate variability. Perhaps the best documented case of retreat of multiple waterfalls across a study area is from Hayakawa and Matsukura (2003); however, this study did not compare waterfall retreat rates to reach-scale or basin-average erosion rates in the same catchment, making it difficult to assess the relative rate of waterfall erosion.

Here, we attempt to quantify the conditions in which waterfalls erode fast or slow relative to waterfall-free reaches through a detailed field study in the southern Sierra Nevada, CA, including both waterfalls within and apart from larger-scale knickzones. We investigate the possibility that waterfall formation (be it via internal or external forcing) allows for tectonically determined erosion rates to be expressed via differences in channel morphologies (e.g., waterfall formation can allow rivers with identical erosion rates to have different reach-averaged slopes) as proposed by Rothman et al. (2023). Given existing data (DiBiase et al., 2015; Mackey et al., 2014; Valla et al., 2010) suggesting that waterfalls erode faster than surrounding waterfall-free reaches (in areas of moderate to large drainage area), we hypothesize that reach-averaged erosion rates should increase with increasing waterfall frequency in a given river reach. Testing this hypothesis requires a reach-based approach rather than investigating a single waterfall. We use concentrations of cosmogenic ^{10}Be found in the bedrock of the river bed to measure local, reach-averaged erosion rates in 10 reaches spread between two rivers with varying waterfall frequency and waterfall morphology. We compare these local erosion rates with basin-averaged erosion rate measurements estimated from detrital sand to assess whether waterfalls amplify or dampen reach-scale erosion

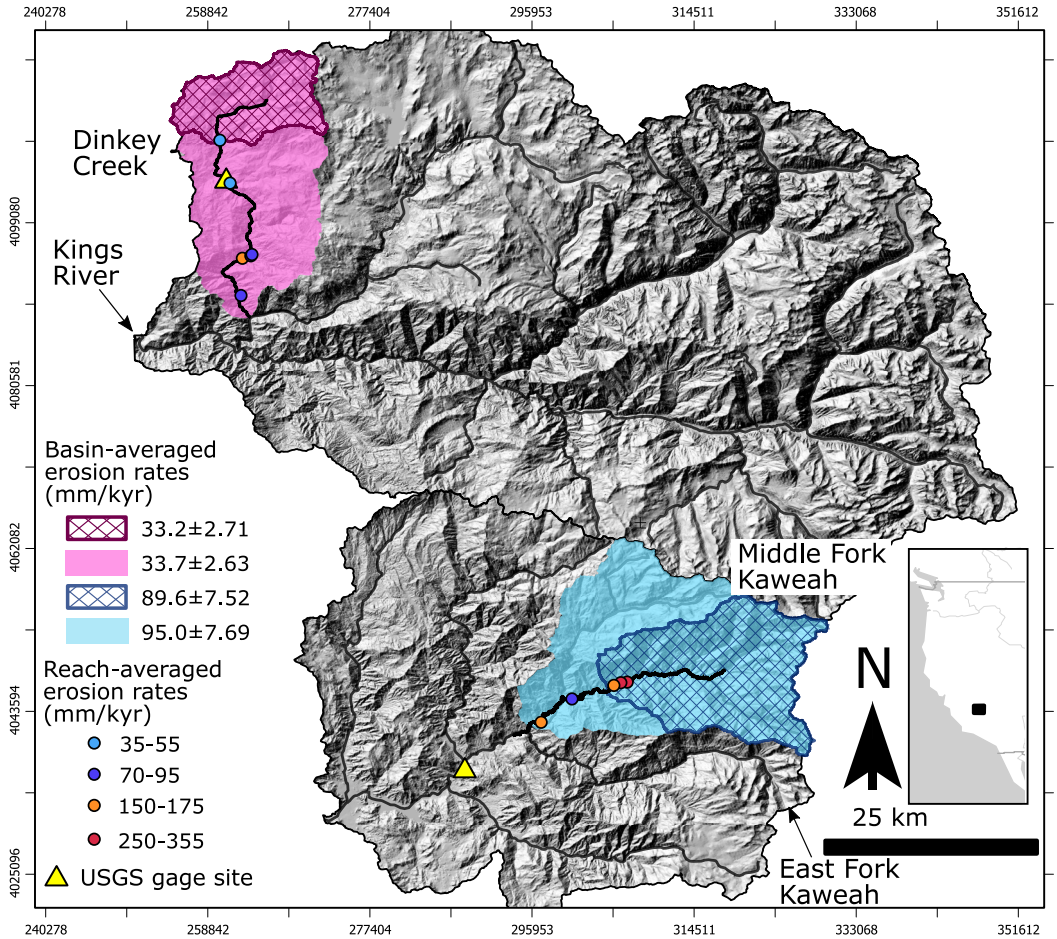

Figure 1. Location map showing the Middle Fork Kaweah and Dinkey Creek watersheds in the Sierra Nevada, CA. Areas upstream of sand collected for basin-averaged erosion rates are shaded and cross-hatched; filled circles mark the locations of reaches sampled for reach-averaged erosion rates.

rates at our field sites. To further explore mechanistic controls on the relative erosion rate between waterfall-rich and waterfall-free reaches, we develop a new process-based model combining waterfall and planar-channel erosion, which we use to explore the conditions under which the presence of waterfalls will increase or decrease reach-scale erosion relative to reaches without waterfalls.

2. Study Area

We examine how waterfall frequency and morphology affect erosion rates in two rivers draining the western slope of the Sierra Nevada in California, USA: Dinkey Creek (a tributary of the North Fork of the Kings River) and the Middle Fork Kaweah (MFK) River (Figure 1, Figures S2–S5 in Supporting Information S1). These rivers represent an ideal setting to test our hypothesis because the study rivers are only ~40 km apart, share a common base level and tectonic history, and are in a mostly homogeneous and resistant lithology (predominately granitic rock) with no major faults and abundant waterfalls (Bateman & Jones, 1972; Matthews & Burnett, 1965; Moore & Sisson, 1987; Sisson & Moore, 2013). The Middle Fork Kaweah has a slightly higher drainage area at our study reaches (213–423 km^2) relative to our Dinkey Creek study reaches (100–301 km^2, Table S1 in Supporting Information S2). Both drainages are composed predominantly of granitic bedrock, with seven of our 10 reaches underlain by uniform granite, and three reaches (MFK21-09, DNK22-03, and DNK21-04) underlain by a mix of granitic and metamorphic bedrock. The MFK and Dinkey Creek receive an average of 1,300 and 1,100 mm of precipitation per year, respectively, which occurs primarily as winter snowfall (Prism Climate Group, Oregon State University, 2024). Mean annual temperatures for the MFK and Dinkey Creek are 6.9 and 9.4°C, respectively (Table S1 in Supporting Information S2). Both basins span ~3 km of relief, allowing temperature and snow

accumulation to vary widely between high and low elevations. While climate is similar between the two basins, over the past 30 years the MFK basin has received greater mean annual precipitation (1,300 mm/yr) than Dinkey Creek (1,100 mm/yr) but lower flood discharges than Dinkey Creek (Table S1 in Supporting Information S2). Higher flood discharges at Dinkey Creek may be due to lower headwater elevation, allowing an earlier spring snow melt and more precipitation as rain. During the Last Glacial Maximum (LGM), the MFK and Dinkey Creek basins were ∼30% and ∼28% glaciated, respectively (Table S1 in Supporting Information S2), with all LGM glaciation above our study reaches (Gillespie & Clark, 2011). Despite previous glaciation of the basin headwaters, optical imagery suggests that most previously glaciated valleys have little to no storage of glacial sediments. We therefore assume minimal input of glacial sediment into the study reaches where we collected detrital cosmogenic samples.

Previous assessment of the influence of waterfall formation on long profile form in Dinkey Creek and the East Fork Kaweah (a tributary of the Middle Fork Kaweah with similar profile form) shows that waterfall frequency is closely correlated with channel slope in Dinkey Creek but only loosely correlated with channel slope in the East Fork Kaweah (Rothman et al., 2023). These differences in longitudinal profile form were attributed to differences in waterfall erosion rate relative to the erosion rates in adjacent, waterfall-free channels, introducing the possibility that slow-eroding, self-formed waterfalls create high-slope knickzones in Dinkey Creek, but fast-eroding, self-formed waterfalls reduce East Fork Kaweah channel slopes. The difference in waterfall erosion speed hypothesized by Rothman et al. (2023) for the East Fork Kaweah and Dinkey Creek represents an opportunity to investigate the drivers of waterfall erosion rates in the field. In this study, we focus on the MFK instead of the East Fork Kaweah, because the MFK has abundant waterfalls and a similar profile to the East Fork Kaweah, but the increased accessibility of MFK facilitates detailed field measurements and sample collection.

3. Assessment of Channel and Basin-Averaged Erosion Rates Using Cosmogenic ^{10}Be

3.1. Approach

In this study, we define waterfalls as bedrock bedforms with a steep face from which water detaches and enters free fall (Groh & Scheingross, 2022). The water reconnects with the river in a downstream plunge pool, which is drilled by the force of the water and sediment impacts descending from the waterfall jet (Scheingross et al., 2017). We only examine waterfalls that erode primarily through plunge-pool drilling (e.g., Howard et al., 1994; Lamb et al., 2007), and we assume that plunge-pool drilling is the main erosional mechanism if a waterfall has smooth, well-abraded bedrock at the waterfall lip and a plunge pool with geometry independent of existing bedrock fracture patterns. While we suggest that the waterfalls we investigate here have self-formed in a massive, resistant lithology, waterfalls can also form in layered rock due to variable lithologic resistance to erosion (Chilton & Spotila, 2022; Frankel et al., 2007; Holland & Pickup, 1976) and some waterfalls erode primarily by undercutting and caprock collapse (Gilbert, 1890; Haviv et al., 2010), gradual detachment of rock from the waterfall face (e.g., Hayakawa & Matsukura, 2010), or toppling along lithologic weaknesses (e.g., Lamb & Dietrich, 2009). This study is not applicable to waterfalls that erode via these mechanisms.

To test whether waterfall occurrence causes reaches to erode faster or slower than the basin-averaged erosion rate, we constrained erosion rates of waterfall-rich channels using cosmogenic radionuclide inventories. Specifically, we examined how local, reach-averaged bedrock erosion rates vary as a function of waterfall frequency within a channel reach by collecting and amalgamating multiple bedrock samples from the active channel (targeting waterfall lips, waterfall faces and plunge pool margins). We compare these local, reach-averaged erosion rates to basin-averaged erosion rates derived from ^{10}Be concentrations in fluvially deposited sand in mainstem channels. We used the ratio of the local, reach-averaged erosion rate (E_{reach_avg}) and the basin-averaged erosion rate (E_{basin_avg}) to define a normalized erosion rate (E_{norm}) representing the erosional efficiency of the reach relative to the basin average.

$$E_{norm} = E_{reach\_avg}/E_{basin\_avg} \quad (1)$$

To test how waterfall abundance and morphology affect bedrock incision rates, we combined our estimates of normalized erosion rate with field and lidar surveys of waterfall and channel morphology across our study reaches. $E_{norm} > 1$ and $E_{norm} < 1$ imply fast and slow waterfall erosion, respectively, but importantly, E_{norm} is not a direct measure of whether waterfall-rich reaches erode fast or slow relative to waterfall free reaches. Such a

direct measurement would require independent measures of erosion rates in both waterfall-rich and waterfall-free reaches. In our field area waterfall free reaches are often mantled in sediment cover, limiting access to the bedrock bed and our ability to measure waterfall-free reach erosion rates with cosmogenic nuclides.

3.2. Methods

3.2.1. Sample Collection and Processing

We gathered samples from 10 different field locations (Figures 1 and 2), selecting areas with different waterfall frequencies based on accessibility and waterfall visibility in satellite imagery and high-resolution topography derived from lidar (Table S2 in Supporting Information S2). All sites featured smooth, polished rock, consistent with erosion via abrasion (as opposed to plucking) and at all sites, the position of the waterfall lip was independent of channel-wide bedrock fractures. At each site, we collected two to four bedrock samples from waterfall lips, waterfall faces and exposed plunge pool margins (Figure 2, Figures S2–S5 in Supporting Information S1, Table S3 in Supporting Information S2). The samples, which were less than 4 cm in thickness, were always taken from the surface of bedrock bed and were collected primarily via hammer and chisel and in some cases (for sites outside of Sequoia National Park) with an angle grinder. Within a reach, we selected specific areas to collect bedrock samples based on proximity to waterfalls, prominence above the water surface at low flows, evidence of fluvial abrasion (i.e., a smooth bedrock surface), and avoidance of surfaces where the intersection of bedrock joints showed evidence of recent block plucking. We also avoided sampling bedrock from plunge-pool floors, where both sediment and water shield bedrock. Samples in each reach were always within 120 m of one another, with the exception of one site (DNK21-0304) where we amalgamated two samples (located within ∼10 m of each other) with a third sample located ∼1 km downstream but in a location with similar reach morphology as the two upstream samples.

We collected four detrital sand samples for basin-averaged erosion rates, two samples each from the mainstem Middle Fork Kaweah and Dinkey Creek (Figure 1, Table S1 in Supporting Information S2). For each river, we collected nested samples, that is, we collected one sample downstream of all study reaches and one sample near the upstream extent of the study reaches, allowing us to test whether different parts of the basin erode at equal rates. In both the upstream and downstream locations, we amalgamated fluvially deposited sand from at least four different deposits, including areas inundated at the time of measurement (during low-flow conditions in the late summer and fall) and from emerged bars that we interpret to be deposited during high flow. When calculating E_{norm} in Equation 1, we always used the basin-averaged erosion rate from the drainage basin with a larger contributing area.

Our sample processing and preparation differed slightly between bedrock collected for reach-averaged erosion rates and sand collected for basin-averaged erosion rates. For bedrock samples, we separately ground and sieved each sample into 106–850 μm particles. We then visually estimated the quartz content in each individual sample using an optical microscope (Table S3 in Supporting Information S2), before creating a single amalgamated sample by combining all bedrock samples from the reach, ensuring an approximately equal quartz contribution from each individual sample. The combined sample with equal quartz content from each individual sample represents an average erosion rate from the acquired samples, and a better estimate of the reach-averaged erosion rate. For detrital sand samples, we dried and sieved sand into 100–500 μm and 500–1,000 μm size fractions and then combined equal masses of each size fraction to protect against a grain-size bias (Lukens et al., 2016). For all samples, quartz purification, chemical preparation and ^{10}Be measurements were made at the Lawrence Livermore National Lab Center for Accelerator Mass Spectrometry. For detrital samples, we considered the influence of shielding from snow, whereas for bedrock samples we calculated shielding from water cover and topography (Text S1, Table S4 in Supporting Information S2). We used CAIRN and LSD Topotools (Mudd et al., 2016, 2023) to assess differences in production rates throughout the basin, and calculated final erosion rates for both detrital and bedrock samples using the LSD calibration (Lifton et al., 2014) in the CRONUS earth calculator (Balco et al., 2008).

3.2.2. Lidar Surveys and Field Data Collection

We measured morphology and sediment conditions at each study reach via lidar analysis and field campaigns conducted in 2020, 2021, 2022, and 2023. For each study reach, we made measurements of channel, waterfall and plunge pool geometry across a 300 m stretch (as measured using the channel centerline in Google Earth) including

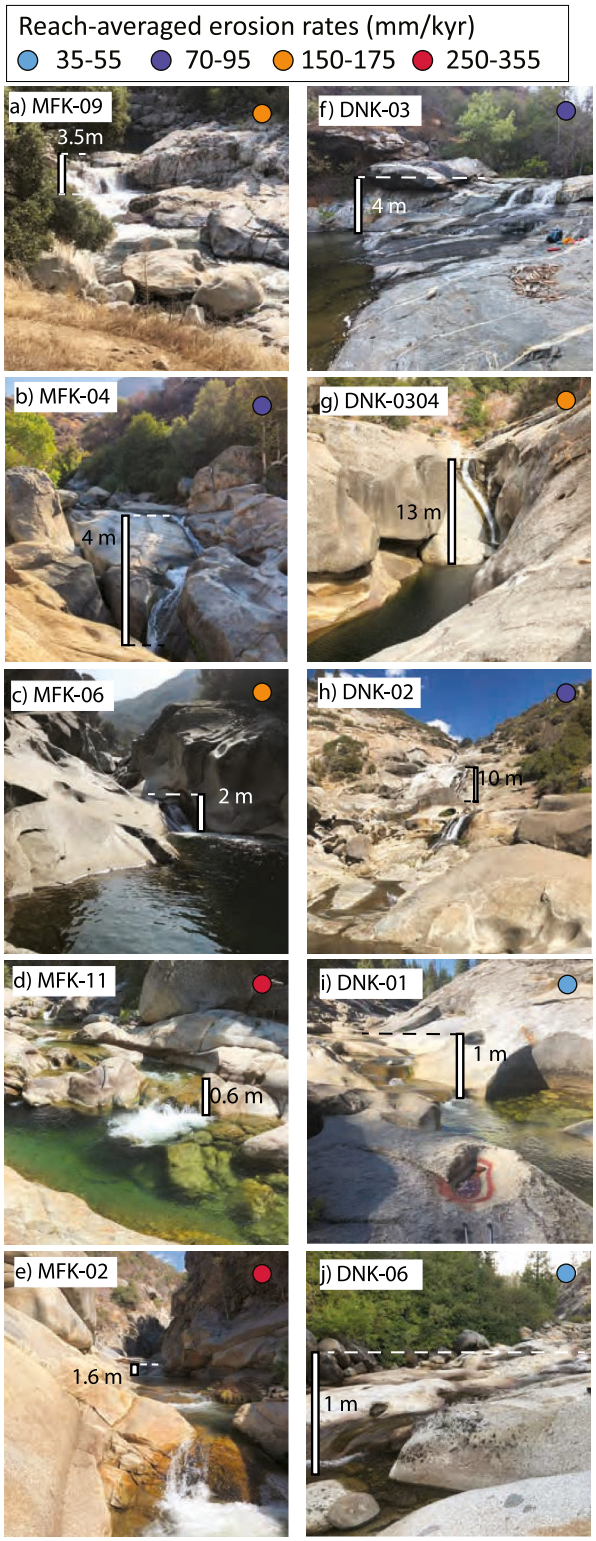

Figure 2. Bedrock sample reaches: (a–e) Middle Fork Kaweah and (f–j) Dinkey Creek, ordered from downstream (top images) to upstream (bottom images) for both rivers. Colored circles in the upper-right corner of each image represent the reach-averaged erosion rate. Scale bars show vertical drop heights for the waterfalls pictured.

and moving upstream from the bedrock sample sites. We measured morphology upstream of the bedrock sample site (as opposed to downstream) based on the assumption of Froude critical or supercritical flow at waterfall lips (Rouse, 1936, 1937), thereby preventing hydraulic communication from areas downstream with our reach of interest. For site DNK21-0304, where one sample was located ~1 km downstream, we combined measurements made across a 100 m stretch at the downstream site and a 200 m stretch at the upstream site.

Many of our study reaches were partially inaccessible on foot. To make consistent measurements along the same channel length at all sites, we used lidar to measure waterfall frequency, channel slope, and waterfall drop height rather than making field measurements. Using Topotoolbox 2 (Schwanghart & Kuhn, 2010; Schwanghart & Scherler, 2014) and a lidar-derived DEM, we extracted the channel profile, and manually identified waterfalls as drops with >1 m drop height over horizontal distances of less than 10 m (Figure S6 in Supporting Information S1). We used lidar-derived profiles to manually measure waterfall drop height as the change in elevation between where the waterfall drop begins (often with a low angle lip feeding into a steeper face) and ends (in a pool with a slope of zero). We measured waterfall frequency across a reach ~300 m long (or roughly 15 times the average waterfall length across both study areas) in order to capture variation in waterfall frequency (Table S5 in Supporting Information S2). Lidar was not available for one of our reaches (DNK22-03). In this case, we identified waterfalls using Google Earth following Rothman et al. (2023) (see Text S4 in Rothman et al. (2023)), and measured drop heights using 10 m DEM in conjunction with visual imagery.

In the field, we measured plunge pool depth, width, and length for accessible waterfalls (Figure S1 in Supporting Information S1, Table S6 in Supporting Information S2). Using a weighted tape measure (with mm precision), we measured pool depth as the maximum distance between the water surface and the pool floor at the time of measurement, focusing on areas close to where the waterfall jet impinges in the plunge pool at high flow. This measurement represents a minimum plunge pool bedrock depth, because most MFK pools and some Dinkey Creek pools were partially filled with sediment at the time of measurement. We defined pool width as the maximum cross-stream distance from the water's edge on one side of the pool to the other, and pool length as the along-stream distance between the water's surface at the waterfall face and the downstream plunge-pool lip (the point at which the channel bed changes from increasing in elevation as the plunge pool shallows to decreasing in elevation in the downstream river reach) (Figure S1 in Supporting Information S1). We measured the plunge-pool width and length using a laser range finder (with cm precision) to identify the maximum distance. Our field observations showed predominately asymmetric pools (i.e., length and width were not the same, in contrast to cylindrical pools often assumed in modeling (e.g., Scheingross & Lamb, 2017), and we therefore estimated pool radius as the minimum value between half pool length and half pool width (Table S6 in Supporting Information S2).

We used additional data to compare water discharge and sediment availability at MFK and Dinkey Creek. We estimated discharge at each of our study reaches using linear drainage-area scaling of discharge reported at USGS gauge 11217000 (Dinkey Creek) and 11209900 (MFK) (Table S7 in Supporting Information S2). We measured grain size at 12 locations in MFK and

six locations in Dinkey Creek via random walk pebble counts with measurement of >100 median grain diameters in all but one case where we measured 50 grains (Table S8 in Supporting Information S2). For both MFK and Dinkey Creek, grain size distributions are relatively constant with distance downstream (Table S9 in Supporting Information S2), allowing us to combine all pebble count data from each river to estimate a single median grain size. We made qualitative observations of the degree of sediment cover on the riverbed throughout all areas surveyed in both Dinkey Creek and MFK.

3.3. Erosion Rate and Channel Morphology Results and Discussion

We find that basin-averaged cosmogenic erosion rates in the MFK (95.0 ± 7.69 mm/kyr and 89.6 ± 7.52 mm/kyr) are significantly faster than in Dinkey Creek (33.7 ± 2.63 and 33.2 ± 2.71 mm/kyr) (Figure 1, Tables S1 and S7 in Supporting Information S2). For both drainages, the nested erosion rates are within error of each other, suggesting uniform erosion throughout both catchments. Although our basin-averaged erosion rates reflect the average landscape erosion rate of the upstream basin, our reach-averaged erosion rates represent the fluvial erosion rate of our study reaches. We find that, with one exception, our reach-averaged erosion rates are all faster than the basin-averaged erosion rate of the landscape. Furthermore, an unpaired t test ($p = 0.05$) shows that reach-averaged erosion rates from bedrock samples in the MFK (which range from 78 mm/kyr to 439 mm/kyr) are, on average, faster than reach-averaged erosion rates in Dinkey Creek (44 mm/kyr to 170 mm/kyr, Figure 3a, Table S4 in Supporting Information S2). Higher reach-averaged erosion rates in the MFK relative to Dinkey Creek may be due to differences in grain size and sediment supply between the rivers, because higher sediment supply and larger grain sizes are predicted to result in higher erosion rates in sediment-poor rivers (Beer & Turowski, 2015; Sklar & Dietrich, 2004). Pebble counts (Table S5 in Supporting Information S2) show smaller median grain sizes (D_{50}) in Dinkey Creek (3.0 cm) relative to the MFK (10.3 cm), and Dinkey Creek had lower sediment cover than the MFK. For example, the MFK had frequent cobble bars and plunge pools typically mantled with sediment, while in Dinkey Creek some plunge pools were baer, and there were few visible sediment deposits in between waterfalls (Figure S7 in Supporting Information S1). These observations are consistent with previous studies in the Shaver Lake upland (e.g., Callahan et al., 2019), which have argued for a tools-limited regime with inefficient erosion in the Dinkey Creek region.

Unlike the dimensional erosion rates, normalized reach-averaged erosion rates (Equation 1) are not significantly different between the MFK and Dinkey Creek (as determined by an unpaired t test, $p = 0.58$), with values ranging from $0.76 < E_{norm} < 3.7$ for the MFK, and $1.2 < E_{norm} < 4.6$ for Dinkey Creek (Figure 3b, Table S7 in Supporting Information S2). The collapse of the reach-averaged erosion rates into the same range of values ($E_{norm} \approx 1$–5) via normalization emphasizes the importance of basin-wide variables (specifically, sediment abundance and size) in setting reach-scale erosion rates and raises the possibility that E_{norm} of waterfall-rich reaches in many rivers may fall within this range. Since $E_{norm} > 1$ indicates that reaches are eroding faster than the basin-average rate, we interpret the predominance of $E_{norm} > 1$ as an indication that waterfalls increase reach-scale erosion rates, at least in the relatively large (>100 km^2) drainage areas we examined here. This result is consistent with previous findings of fast waterfall erosion at large drainage areas (Crosby & Whipple, 2006; DiBiase et al., 2015; Raming & Whipple, 2022). Because the location of our study reaches far from channel heads, our data cannot be used to test the associated idea that waterfall erosion slows and may even stall at low drainage areas.

We use the normalized erosion rates to examine the influence of reach-scale morphology on reach-scale erosion rates. Several metrics that are often assumed to scale with reach-scale erosion rates are not significantly correlated with E_{norm} in our data set (Figure 4). For example, while channel erosion rates often scale with stream power (Finnegan et al., 2008; Lague, 2014), we find no significant trend between stream power and E_{norm} (using Pearson's correlation coefficient, ρ, Figure 4a). Other studies show that in high-slope knickzones, retreat rates scale with drainage area (e.g., Crosby & Whipple, 2006) or slow at a drainage area threshold (e.g., Raming & Whipple, 2022); however, our results show no significant relationship between drainage area and E_{norm} (Figure 4b). Channel width has also been shown to decrease with increasing erosion rates (e.g., Duvall et al., 2004); however, our results show no significant relationship between reach-scale erosion rates and reach-averaged channel width (Figure 4c). We also investigated the influence of waterfall and plunge-pool geometry on reach-scale erosion rates. Although plunge-pool erosion rates are predicted to increase with waterfall drop height and decrease with greater pool depth and radius (Scheingross & Lamb, 2017), our results show no significant

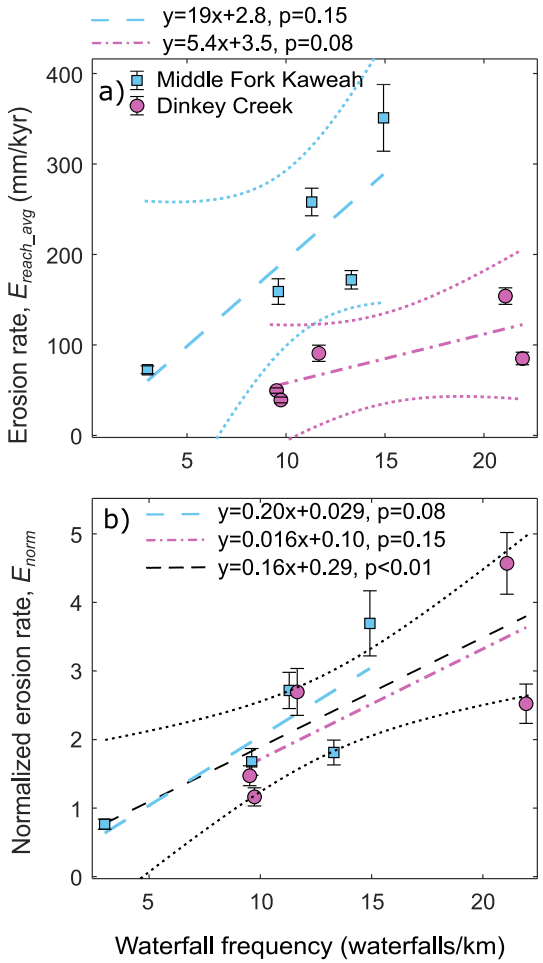

Figure 3. Waterfall frequency versus (a) ^{10}Be-derived reach-averaged erosion rates (E_{reach_avg}) for bedrock reaches sampled, and (b) reach-averaged erosion rates normalized by their respective basin averaged erosion rates (E_{norm}, Equation 1). For both plots, separate best-fit linear models for Dinkey Creek (pink line) and Middle Fork Kaweah (blue line) are shown with p values for the slope of the line. For the normalized data, the black dashed line shows the best-fit linear trend for the entire data set (Dinkey Creek and MFK data combined). While the data sets are small on their own, the MFK and Dinkey Creek data sets display the same trend. Thus, the relationship becomes more significant when the data sets for the MFK and Dinkey Creek are combined in panel (b). The dotted lines represent 95% confidence intervals, and in panel (b) the confidence intervals for the individual MFK and Dinkey Creek relationships are omitted for clarity. The error bars represent the measurement and methodological error of the cosmogenic erosion rate measurements.

correlation between reach-averaged drop height, pool depth, and pool radius with E_{norm} (Figures 4d–4f). When treated individually, MFK and Dinkey Creek display different correlations between E_{norm} and pool depth and reach width (ρ and p values are available for the individual and combined data sets in Table S10 in Supporting Information S2), which may indicate that under different sediment conditions, channel form has a different influence on erosion rate (elaborated on in Text S2 in Supporting Information S1). Furthermore, we acknowledge that the trends (or lack thereof) shown in Figure 4 are potentially sensitive to measurement error. Waterfalls and plunge pools in particular are irregular landforms from which it can be difficult to obtain objective geometric measurements. However, in the case of the data presented in Figure 4, the range of reported waterfall drop heights (2.2–8.5 m, Table S7 in Supporting Information S2), plunge-pool radii (1.0–8.5 m, Table S7 in Supporting Information S2), and plunge-pool depth (1.0–4.0 m, Table S7 in Supporting Information S2) are all large. Thus, even if uncertainty on the order of ∼1.0 m exists in our geometric measurements, the lack of a statistically significant trend between geometric variables and normalized reach-scale erosion rates is still meaningful.

Of all the variables we examined, the only significant correlation we found was between waterfall frequency and E_{norm} (p = <0.01, Figure 3b). Our data show that the fastest eroding reaches have high waterfall frequencies (10–21 waterfalls/km), whereas the site with the lowest waterfall frequency (MFK-04, ∼2 waterfalls/km) was the only site with $E_{norm} < 1$. Fitting a linear relationship to our E_{norm} versus waterfall frequency data demonstrates that there is a significant positive relationship between these variables ($p < 0.01$), and highlights the fact that waterfall erosional processes can lead to faster reach-scale erosion rates (relative to the basin average erosion rates) in reaches with greater than ∼5 waterfalls per km. Furthermore, while we could not test the reach-averaged erosion rate of waterfall-free reaches (as they tended to be covered with sediment limiting our ability to sample the bedrock bed), the best fit linear model between E_{norm} and waterfall-frequency (Figure 3b) infers that waterfall-free reaches should erode both slower than the basin average and slower than waterfall-rich reaches.

Our results show that waterfall-rich channels erode faster than both waterfall-free reaches and the basin average rate, with waterfall frequency being the most important variable predicting normalized erosion rates. This conclusion suggests that, without changing relief or length, a reach could erode at five times its planar-bed erosion rate by forming frequent waterfalls along its length. Following this logic, processes resulting in the formation of multiple waterfalls (e.g., the formation of waterfalls and bedrock cyclic steps as bedrock bedforms (e.g., Baynes, Lague, & Kermarrec, 2018; Groh & Scheingross, 2022; Izumi et al., 2017)) should yield faster reach-scale erosion rates than processes that result in the formation of a single waterfall (e.g., accumulated slip along a fault, Malatesta & Lamb, 2018). We investigate this possibility further in Section 5.

4. Discussion: Implications for Long-Profile Evolution in Waterfall Rich Reaches

Rothman et al. (2023) used a modified stream power model to argue that river profile form and evolution are influenced by both waterfall development, and whether waterfalls erode "fast" or "slow" relative to waterfall-free reaches. This previous modeling effort suggests that elements of the East Fork Kaweah River (a tributary of the MFK) and Dinkey Creek are consistent with fast and slow waterfall erosion, respectively. The new cosmogenic data presented here provide an opportunity to field test some of our previous modeling predictions and show consistency with the Rothman et al. (2023) fast waterfall model.

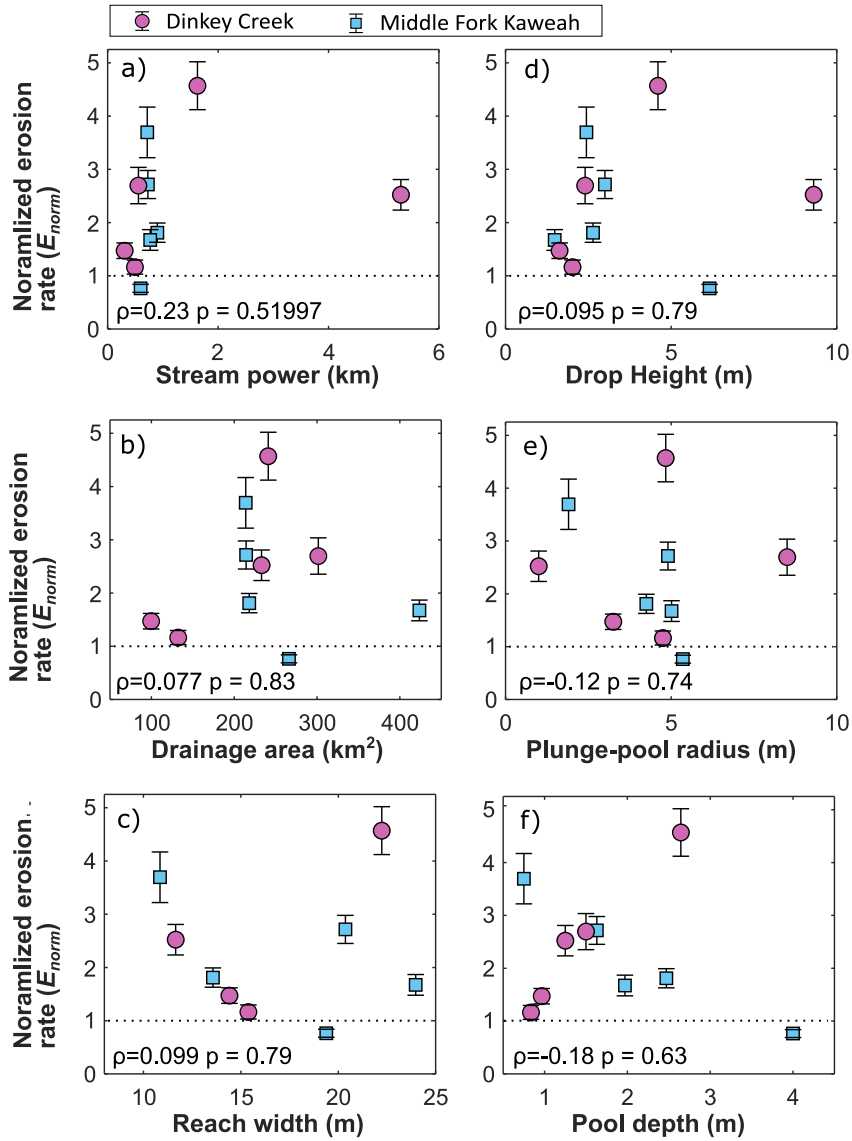

Figure 4. Normalized channel erosion rates as a function of (a–c) channel metrics including (a) stream power ($S \times A^{.0.5}$ where S is local channel slope and A is drainage area), (b) drainage area, (c) reach-averaged width, calculated using a 10-year return period discharge and channel parameters (Text S1 in Supporting Information S1) and (d–f) waterfall morphology including (d) reach-averaged drop height, (e) reach-averaged plunge-pool radius and (f) reach-averaged plunge pool depth. In all panels, the dotted line at $E_{norm} = 1$ marks the transition between fast and slow reach-averaged erosion rates. Each plot displays the Pearson correlation coefficient (ρ) and corresponding p-value for the relationship between that variable and E_{norm}.

The Rothman et al. (2023) fast waterfall model predicts that when channels steepen above the critical slope necessary for waterfalls to self-form (~3%–7%, Groh & Scheingross, 2022), a zone of dynamic equilibrium forms in which the channel cyclically aggrades and over-erodes to keep slopes fluctuating around the critical value for waterfall self-formation. Four of the five bedrock sample sites in the MFK had $E_{norm} > 1$, indicating fast waterfall erosion relative to waterfall-free channels. Furthermore, these sites were not positioned in high-slope reaches resembling knickzones; rather, the bedrock sample sites occurred along a reach of near-constant slope of 4.1% (Figure 5a). We interpret the existence of this relatively constant-slope reach, the magnitude of the slope within the 3%–7% range where waterfalls are speculated to self-form (Groh & Scheingross, 2022), and the cosmogenic data implying fast waterfall erosion to all be consistent with the Rothman et al. (2023) model predictions for a fast waterfall dynamic zone. The strong correlation between waterfall frequency and reach-averaged erosion rates and

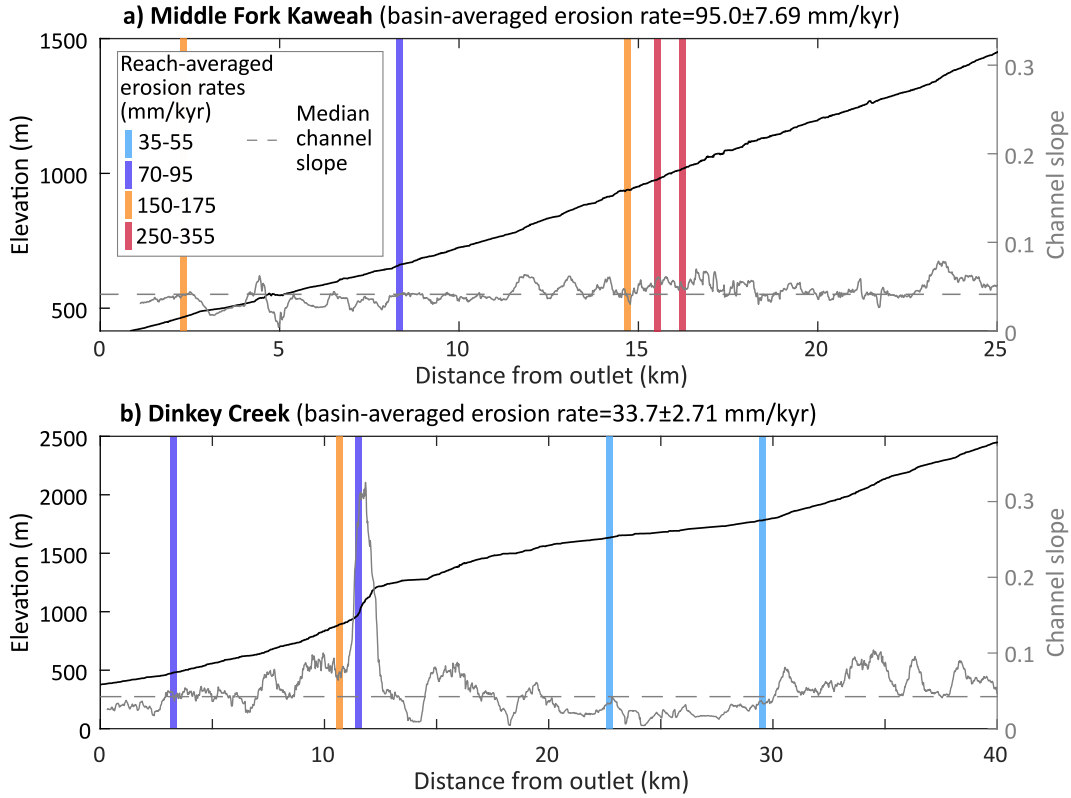

Figure 5. Elevation and slope profile of (a) MFK and (b) Dinkey Creek. Bars show bedrock sample sites and are colored by the reach-average erosion rate. The dashed line shows the median channel slope. In both plots, the channel slope is a running mean averaged over a 0.5 km moving window.

the lack of correlation between stream power and reach-averaged erosion rates in the MFK therefore provide the best evidence to date that waterfall formation and erosion can shape longitudinal profiles over km length scales.

Rothman et al. (2023) suggested that Dinkey Creek hosts slow waterfall erosion, which could be responsible for the large knickzone at ~12 km upstream of the Dinkey Creek outlet at site DNK-02 (Figure 5b). However, the cosmogenic data presented here show that all bedrock sample sites in Dinkey Creek erode faster than the basin-averaged erosion rate, implying fast waterfall erosion. This result introduces the possibility that Rothman et al. (2023) misinterpreted the Dinkey Creek long profile signal; however, there are several explanations for the $E_{norm} > 1$ measurements in Dinkey Creek that allow for consistency with the Rothman et al. (2023) model results. First, it is possible that the Dinkey Creek long-profile morphology is influenced by both rock-strength heterogeneity (which occurs on too fine a scale to be captured by existing geologic maps) and fast-waterfall erosion that superimpose to make a complicated long-profile form. In this case, the slope fluctuations (including the high channel-slope at site DNK-02) may reflect variations in rock strength. It is also worth noting that, with the exception of the two largest high-slope knickzones on Dinkey Creek, much of the rest of the channel fluctuates around a median slope of 4.2%, similar to the MFK and consistent with the Rothman et al. (2023) fast waterfall model. Alternatively, Dinkey Creek may be experiencing a transient response to late Cenozoic uplift (Beeson & McCoy, 2022; Stock et al., 2005; Wakabayashi, 2013). In the Rothman et al. (2023) model, slow waterfalls will erode faster than the basin average where they occur in transient knickzones; therefore, it is feasible for the waterfalls we sampled to have $E_{norm} > 1$ while still slowing the knickzone erosion rate from what it would be without waterfalls. Finally, it is possible that the Dinkey Creek hillslopes are out of equilibrium with channel incision (e.g., Callahan et al., 2019; Stokes et al., 2023), and that basin-averaged erosion rates thus give little insight into channel incision rates. If basin-averaged erosion rates do not reflect channel incision rates, then it is not possible to assess the erosion rate of Dinkey Creek waterfalls relative to planar-channel incision. While determining which, if any, of the above three possibilities is occurring in Dinkey Creek requires additional work which is beyond the scope of this study, we emphasize that these results still allow for consistency with the

Rothman et al. (2023) model and highlight the range of complicating factors that can occur even in a relatively well-constrained field setting.

Finally, inspection of the samples near the largest Dinkey Creek knickzone provides additional insights into controls on reach-scale erosion rates. Samples DNK-02 and DNK-0304 were sampled ~300 m apart, but DNK02 was in the high-slope knickzone (average channel slope of 0.35), whereas DNK-0304 was in a lower-sloping reach (average channel slope of 0.10). In a stream power analysis, this higher-slope sample site would be expected to have a higher local erosion rate than the lower-slope site; however, our results show the opposite, with the steep knickzone site (DNK-02) eroding a factor of ~2 slower than the less-steep site (DNK-0304) (Figures 2 and 5). Based on our field observations, we posit that this decrease in erosion rate at steep slopes may be due to a switch from fluvial abrasion at moderate slopes to weathering and rockfall processes at higher slopes. Field visits to DNK-02 showed little fluvial canyon incision into the surrounding landscape, the presence of very small plunge pools (average radius = 1 m), large waterfall drop heights (average of 6.3 m) and large bedrock slabs that appeared to be detaching from the steep slopes adjacent to the channel (Figure 2h). This field evidence suggests that limited plunge pool incision or other fluvial abrasion occurs in this reach, and that erosion may instead occur primarily through bedrock weathering and rockfall. In contrast, field visits to site DNK-0304 revealed deep plunge pools and fluvially abraded rock (Figure 2g). The high slope but moderate erosion rate of DNK-02 demonstrates that channel slope may not be an important indicator of erosion rates in cases where there is little evidence of extensive fluvial abrasion and incision.

5. Modeling Reach-Averaged Erosion Rates in Waterfall-Rich Channels

Our field data suggest that, at least for the MFK and Dinkey Creek, waterfall-rich reaches erode faster than the basin-averaged erosion rate, and reach-averaged channel erosion rates increase with waterfall frequency (Figure 3). While reach-averaged erosion rates in reaches with waterfalls likely depend on a variety of factors (e.g., Scheingross & Lamb, 2017; Sklar & Dietrich, 2001), the complexity of erosion in natural channels and the overwhelming influence of waterfall frequency in our data make it difficult to gain further insight into the sensitivity of reach-averaged erosion rates using our field data alone. In this section, we use physics-based models to explore the conditions when waterfall development increases or decreases reach-scale erosion rates. We combine existing planar channel (Lamb et al., 2008) and waterfall bedrock erosion theory (Scheingross et al., 2017) into a new reach-averaged erosion model that describes how channels erode by a combination of waterfall and non-waterfall erosional mechanisms. We then examine the effectiveness of the model by entering parameters for our Dinkey Creek and MFK study reaches and comparing the predicted erosion rates to our cosmogenic-derived measurements (without using field measurements or reach-averaged erosion rates to tune our model). Finally, we explore how changes in waterfall and channel geometry, sediment supply, water discharge, and grain size influence the relative erosion rates of waterfall-rich and waterfall-free channels.

5.1. Model Methods: Approach and Development

While models exist for fluvial bedrock incision in planar reaches (e.g., Chatanantavet & Parker, 2009; Lamb et al., 2008; Sklar & Dietrich, 2004; Zhang et al., 2015), and waterfall erosion and retreat (e.g., Crosby & Whipple, 2006; Hayakawa & Matsukura, 2003; Lamb & Dietrich, 2009; Scheingross & Lamb, 2017), no model combines both planar bedrock incision and waterfall erosion. Here we develop a "Combined Processes Model" which predicts the total erosion from both waterfall plunge-pool and planar-channel abrasion (Figure 6a). In this model, we assume that waterfall-rich river reaches are made of alternating planar channels (with erosion rates predicted by the total load model (Lamb et al., 2008)) and channels with waterfalls and plunge pools (with erosion predicted following Scheingross and Lamb (2017)). Our model assumes that reach geometry is constant through time, that planar-channel reaches have constant width and slope, and that each waterfall plunge-pool system within a reach has identical dimensions (Figure 6a).

To predict the instantaneous reach-averaged erosion rate of a channel with both waterfall and planar components ($E_{combined}$) we calculate the spatially weighted average of plunge-pool vertical erosion (E_{wf_vert}), plunge-pool lateral erosion (E_{wf_lat}) and erosion in planar reaches without waterfalls (which we refer to as total load abrasion, E_{tl})

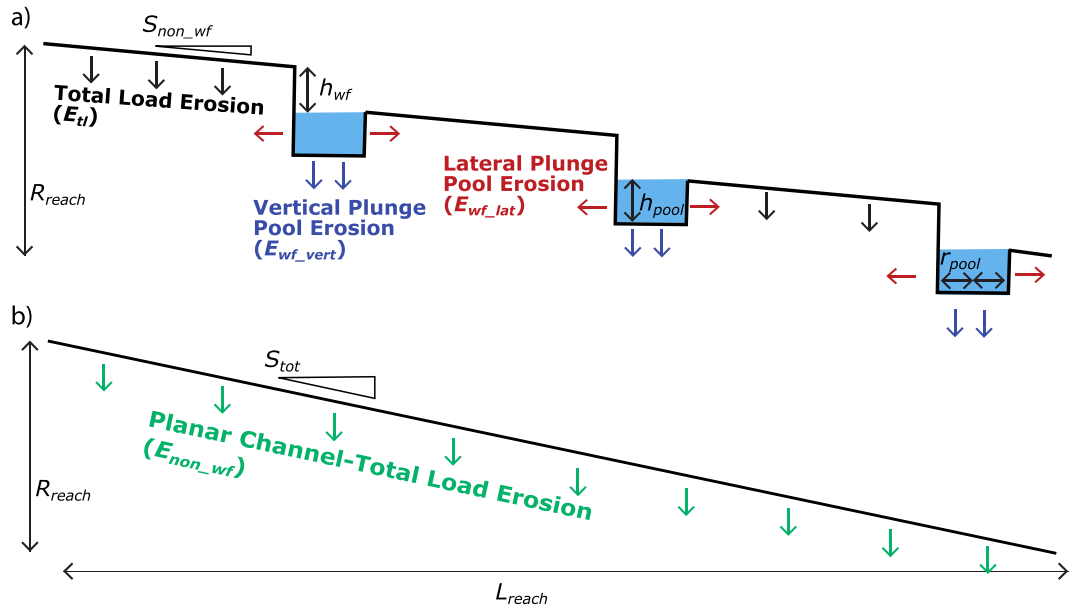

Figure 6. (a) Diagram of the combined model with total load erosion (Lamb et al., 2008) acting on planar portions, and waterfall vertical and lateral erosion (Scheingross & Lamb, 2017) acting on plunge pools. (b) Diagram of a waterfall-free reach with a planar channel and total load erosion (Lamb et al., 2008) throughout.

$$E_{combined} = \frac{[E_{wf\_vert} \cdot r_{pool} \cdot 2 \cdot n_{wf}] + [E_{wf\_lat} \cdot h_{pool} \cdot 2 \cdot n_{wf}] + [E_{tl} \cdot (L_{reach} - (r_{pool} \cdot 2 \cdot n_{wf}))]}{L_{reach}}. \quad (2)$$

In Equation 2, r_{pool} and h_{pool} are the reach-averaged plunge-pool radius and depth, respectively, n_{wf} is the number of waterfalls in the reach, and L_{reach} is the total reach length (Figure 6). The three terms in square brackets in Equation 2 numerator represent the 1D channel erosion rate via vertical plunge-pool erosion, lateral plunge-pool erosion, and total load abrasion, respectively. Note that the total length along which erosion occurs is longer than the reach length because plunge pools erode both vertically and laterally. The factor of two present in the first and third terms in brackets in Equation 2 represents that the length of a plunge pool is two times its radius, and the factor of two in the second term in brackets exists following the assumption that a plunge pool has two walls that erode laterally in our 1D model (Figure 6). Our model assumes zero lateral erosion along the portion of the waterfall face exposed above the plunge-pool water surface, and neglects accelerated erosion immediately upstream of the waterfall lip (Haviv et al., 2006).

We solve for planar bed erosion, E_{tl}, following Lamb et al. (2008) (their Eq. 19) and for plunge-pool erosion components E_{wf_vert} and E_{wf_lat} following Scheingross and Lamb (2017) (their Eq. 6a and 6b, respectively). In both theories, bedrock erosion is predicted by estimating the concentration and velocity of single-sized sediment particles near the bedrock under specified hydraulic conditions. To calculate waterfall erosion rates, we slightly alter the underlying plunge-pool sediment-transport model (Scheingross & Lamb, 2016) by setting the tailwater depth (Eq. 11 in Scheingross & Lamb, 2016) equal to the flow depth in the planar channel. Solving for E_{tl} requires inputs of six parameters describing the sediment and water discharge in the study reach during a given flood: the planar-channel slope (S_{non_wf} in Figure 6a), characteristic sediment size (D_{50}), sediment supply (Q_s), water discharge (Q_{w_site}), as well as reach-averaged channel width and reach-averaged channel depth (established using lidar-based measurements, Text S3 in Supporting Information S1). Solving for E_{wf_vert} and E_{wf_lat} requires the same parameters needed for E_{tl}, as well as reach-averaged waterfall drop height, plunge-pool radius, and plunge-pool depth. Both waterfall and total load abrasion also require constants for bedrock properties (bedrock tensile strength and Young's Modulus), sediment density, and fluid properties (fluid density, kinematic viscosity, and von Kármán's constant).

5.1.1. Site-Specific Model Inputs

Before exploring the parameter space predicted by the Combined Processes Model, we first assess model accuracy by comparing our reach-averaged bedrock erosion rates in MFK and Dinkey Creek (Figure 3a) to Combined Processes Model erosion-rate predictions made with parameters from those sites (without tuning our model with our ^{10}Be-derived erosion rates). Comparing instantaneous erosion rates predicted by Equation 2 to erosion rates measured via cosmogenic nuclides is not a straightforward task. Equation 2 requires input of high temporal resolution data on changes in water and sediment flux, grain size, plunge pool and channel geometry and more, which is not feasible to obtain over the millennial timescales cosmogenic erosion rates integrate. Thus, we make several approximations, as described below, to compare Equation 2 predictions to our cosmogenic-derived erosion rates.

First, we assume that reach geometry, waterfall geometry, waterfall frequency and sediment size are constant through time, and that we can accurately represent erosion using reach-averaged field variables (i.e., a single, reach-averaged value of channel width, waterfall drop height, plunge-pool radius and plunge-pool depth) and a single grain size which we set equal to the D_{50} of the channel of interest (Table S7 in Supporting Information S2). We assume that waterfalls continuously migrate upstream (Baynes, Lague, Attal, et al., 2018; Izumi et al., 2017); thus, both waterfall and total load erosional processes influence local erosion rates in all parts of the channel, independent of where waterfalls are currently positioned in the MFK and Dinkey Creek. Running the Combined Processes Model also requires inputting the slope of the planar portion of the channel between waterfalls (S_{non-wf}) (Figure 6a), which we estimate as

$$S_{non-wf} = \frac{R_{reach} - (h_{wf} \cdot n_{wf})}{(L_{reach} - (r_{pool} \cdot 2 \cdot n_{wf}))} \tag{3}$$

where R_{reach} is the relief from the total reach.

Second, we assume that the integrated erosion recorded by our cosmogenic nuclide data can be approximated to occur through a 10-year recurrence interval flood. We use a 10-year flood as a characteristic flood following the idea that in steep drainages, large floods are often required to mobilize enough sediment to create significant erosion (Turowski et al., 2013) and that waterfall plunge pools are typically filled with sediment for discharges below the 10-year return period (Scheingross & Lamb, 2021). Furthermore, for the case of the MFK and Dinkey Creek, using a larger-magnitude flood would submerge some waterfalls, violating the underlying assumption in the Scheingross and Lamb (2017) model. We calculate the 10-year flood water discharge at each of the bedrock study reaches (Q_{w_site}) using historic gage records scaled by drainage area

$$Q_{w\_site} = Q_{w\_gage} \cdot \frac{A_{site}}{A_{gage}} \tag{4}$$

where A_{site} and A_{gage} are the drainage areas at the sample site and discharge gage, respectively, and Q_{w_gage} is the discharge at the gage (Table S7 in Supporting Information S2). We combine the 10-year discharge with a flow-resistance empiricism (using D_{84} as the roughness element) (Ferguson, 2007) and lidar to estimate flow depth and wetted channel width (Text S3 in Supporting Information S1).

We estimate the sediment supply of the 10-year flood (Q_s) using the long-term basin-averaged erosion rates derived from our detrital cosmogenic nuclide samples (E_{basin_avg}).

$$Q_s = \frac{E_{basin\_avg} \cdot A_{site}}{I_f} \tag{5}$$

where I_f is an intermittency factor that we set equal to 1% (~3.5 days; changing I_f had little effect on model fit, Figure S8 in Supporting Information S1). Equation 5 thus assumes that the total sediment flux transported in a characteristic 10-year flood is equal to the average annual volume of sediment produced by the basin, given an erosion rate equal to that measured by the basin-averaged cosmogenic nuclide samples. This approach follows the idea that, because the frequency-magnitude distribution of flood and erosion events is heavy-tailed (e.g., DiBiase & Whipple, 2011; Lague et al., 2005), the mean-annual erosion rates recorded by basin-averaged cosmogenic

rates should be skewed toward less-frequent erosive events. We emphasize that the basin-averaged erosion rates (derived from ^{10}Be accumulation in detrital sands) are an independent input for sediment flux relative to the reach-averaged erosion rates we are using to test the accuracy of Equation 2.

Using our estimates for the water discharge and sediment flux for a 10-year return flood as inputs into the Combined Processes Model (Equation 2) yields an instantaneous erosion rate for the 10-year event. To compare instantaneous erosion rate predictions with millennium-scale cosmogenic erosion rates, we assume that erosion-producing floods occur once every 10 years and last 3.5 days. We estimate the time-averaged erosion rate, $E_{combined\_time\_avg}$, as

$$E_{combined\_time\_avg} = \frac{E_{combined} \cdot If}{P_{return}} \quad (6)$$

where P_{return} is the 10-year flood return interval.

We acknowledge that these model inputs are simplified in that they are temporally constant and we limit the distribution of flood magnitudes and sediment fluxes that contribute to reach-scale erosion; however, the full frequency-magnitude distribution of floods and time-dependent input variables needed to more accurately test our model against cosmogenic nuclide-derived erosion rates are impossible to constrain given current knowledge. We emphasize that using these approximations allows a comparison between our field-measurements and model predictions at a proof-of-concept level, which has not previously been done for the Combined Processes Model or for either of its component parts (i.e., the Lamb et al., 2008; Scheingross et al., 2017 models). Furthermore, our simplified inputs allow us to carefully examine the influence of each input variable (in Section 5.3) and inform future work which can address how cosmogenic erosion rates reflect a time-average of a broad variety of erosive events.

5.2. Comparison Between Model-Predictions and Field-Measurements

With the exception of one outlier (DNK-02, discussed below), our results show that the Combined Processes Model yields predictions within a factor of two of the range of the cosmogenic nuclide-derived reach-averaged erosion rates in Dinkey Creek and within a factor of five of the reach-averaged erosion rates in the MFK (Figure 7a, Table S7 in Supporting Information S2). Furthermore, the model-predictions agree with field data in predicting higher erosion rates in the MFK relative to Dinkey Creek, and model predictions have a statistically significant positive relationship with field-measured erosion rates ($\rho = 0.85$, $p = 0.004$, Figure 7a). This positive correlation indicates that the Combined Processes Model has a statistically meaningful use in determining which reaches have higher erosion rates. Furthermore, this correlation between predicted and measured values for the Combined Processes Model is higher than the correlation predicted by the total load model or waterfall plunge-pool model in isolation (Figures 7b and 7c), thereby highlighting the importance of including both planar fluvial erosion and waterfall erosion processes in model predictions.

In the correlation estimates above, we excluded one outlier (DNK-02) predicting an erosion rate >600% higher than any other erosion rate prediction (Figure 7a. Table S7 in Supporting Information S2). As previously mentioned (Section 4), this reach was anomalously steep (average channel slope 0.35 relative to an average slope of 0.049 in other sites) with high drop heights and minimal plunge-pool development (Figure 2, Tables S6 and S7 in Supporting Information S2). The strong disagreement between model predictions and cosmogenic-measured erosion rates at DNK-02 is consistent with our interpretation in Section 4 that erosion at DNK-02 is dominated by processes not included within the Combined Processes Model (e.g., weathering and collapse of the waterfall face).

We posit that the decreased accuracy of model predictions in the MFK relative to Dinkey Creek may stem from differences in sediment cover between these two rivers. While study reaches in Dinkey Creek had abundant bedrock exposure (e.g., Figure S7 in Supporting Information S1, Movie S1), the MFK had abundant sediment cover (Movie S2) and study reaches often displayed large (>1 m diameter) boulders covering parts of the channel and frequent paleo-plunge pools (which we define as >1 m deep pools along the channel thalweg that lacked a corresponding waterfall (Figure S9 in Supporting Information S1)). The presence of paleo-plunge pools violates our assumption that a planar channel bed between waterfalls and paleo plunge pools may serve as locations to collect sediment covering the bedrock bed. This increased cover should reduce erosion rates in reaches between

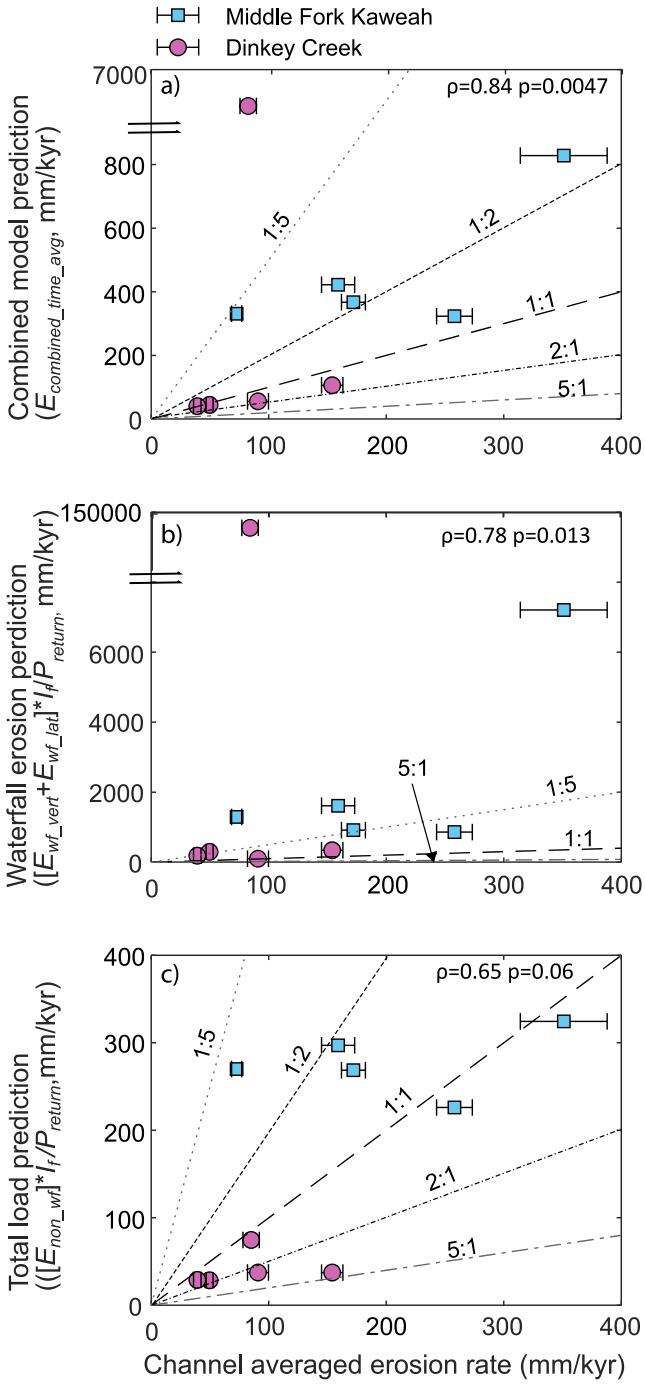

Figure 7. Measured reach-averaged erosion rates versus time-averaged erosion predictions from (a) combined model predictions ($E_{combined\_time\_avg}$), (b) waterfalls only where I_f is the intermittency factor and P_{return} is the recurrence interval of the flood (10-year) and (c) waterfall-free from the total load model (E_{non_wf}) × I_f/P_{return}. In panels (a) and (b), site DNK-02 is an outlier and shown on a split axis. The diagonal lines indicate the accuracy of model predictions located near them and the error bars represent the measurement and methodological error of the cosmogenic erosion rate measurements.

waterfalls relative to our Combined Processes Model predictions and is consistent with the over-prediction of erosion rates with the Combined Processes Model in MFK (Figure 7a). This idea is supported by model results of the Combined Processes Model with planar-bed erosion set to zero (Figure S10 in Supporting Information S1). When planar-bed erosion is set to zero, the Combined Processes Model predicts that four out of five MFK model predictions are within a factor of two of the erosion rate measurements. On the other hand, the Dinkey Creek estimates are less accurate, with three estimates falling to almost one fifth of the cosmogenic-measured erosion rate estimate, which is consistent with our field observations of minimal sediment cover in Dinkey Creek.

Overall, we interpret the positive correlation between model predictions and our cosmogenic measurements of reach-averaged erosion rates to indicate the success of the Combined Processes Model at the proof-of-concept level. While the model may not estimate accurate erosion rates, the Combined Processes Model provides an easy way to estimate differences between reach-scale erosion rates in waterfall-rich channels. Moreover, the agreement between model-predictions and reach-averaged field measurements within a factor of five is reasonable, given the assumptions required to make model predictions (e.g., assuming all erosion occurs in a 10-year return flood due to a lack of data on water and sediment fluxes over the millennial timescales recorded by the cosmogenic-nuclide derived erosion rates). Thus, we argue that the predictive value of the Combined Processes Model in identifying differences in reach-averaged erosion rates between reaches justifies using the model to explore the sensitivity of reach-averaged erosion rates to changing sediment and water discharge, and waterfall and channel geometry, as we do below.

5.3. Exploration of the Combined Processes Model

5.3.1. Methods

We now use our Combined Processes Model to identify how differences in channel morphology, water discharge and sediment flux influence reach-averaged erosion rates. To determine how waterfalls alter erosion rates relative to waterfall-free channels, we use the Combined Processes Model to predict reach-scale erosion as a function of waterfall frequency using the MFK as a reference site (Table S11 in Supporting Information S2). Each model run consists of a 300 m long channel with 22 m of relief partitioned into 20 m of waterfall relief and 2 m of planar-channel relief (e.g., Figure 6a). We explore the role of waterfall frequency in altering erosion rates by performing different model runs with waterfall relief divided into either one, two, four, six, or eight waterfalls with drop heights of 20, 10, 5, 3.3, or 2.5 m, respectively. Because both plunge-pool depth and radius have been suggested to scale with waterfall drop height (Scheingross & Lamb, 2017), we scale plunge-pool depth and radius using the best fit linear relationship with drop height from our field-surveyed data (Figure S11 in Supporting Information S1). These conditions cause channels with higher waterfall frequency to have shorter drop heights, smaller pool radii, smaller pool depths and a greater S_{non_wf} (due to the increased cumulative length of plunge pools, Equation 3).

For all model runs, we present both model results as dimensional (Figure S12 in Supporting Information S1) and non-dimensional (Figure 8) erosion rates. We non-dimensionalized erosion rates by normalizing Combined Processes Model predictions of erosion rate by the erosion rate of a "non-waterfall"

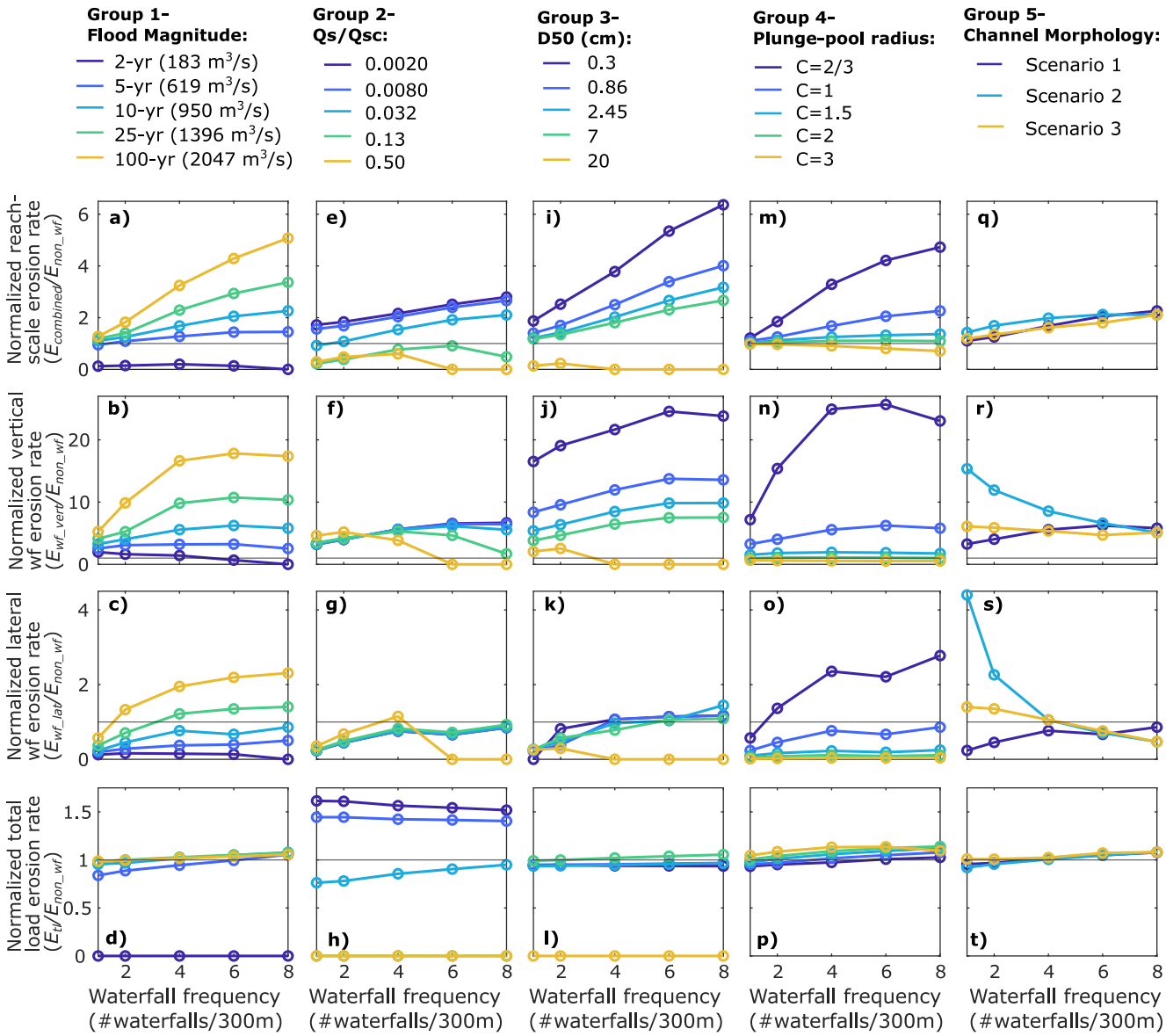

Figure 8. Model predictions under (a–d) varying flood magnitude, (e–h) varying Q_s/Q_{sc}, (i–l) varying D_{50}, (m–p) varying plunge pool radius, and (q–t) varying channel morphology. (a, e, i, m, q) Combined model erosion predictions ($E_{combined}$) normalized by total load model predictions in a waterfall-free channel (E_{non_wf}). (b, f, j, n, r) Vertical waterfall erosion rate (E_{wf_vert}) normalized by E_{non_wf}, (c, g, k, o, s) lateral waterfall erosion rate (E_{wf_lat}) normalized by E_{non_wf}, and (d, h, l, p, t) and total load erosion rate in the planar reaches between waterfalls (E_{tl}) normalized by E_{non_wf}.

channel (E_{non_wf}), estimated using the total load model applied across a channel of the same relief with no waterfalls (Figure 6b). We perform five groups of model runs exploring how erosion rates vary as a function of water discharge (Group 1), the sediment supply to sediment transport capacity ratio (Q_s/Q_{sc}) (Group 2), median grain size (Group 3), plunge pool radius (Group 4), and channel morphology (Group 5), with all other parameters held constant at the MFK reference values (Table S11 in Supporting Information S2) unless otherwise noted. In all model runs, we calculate the sediment transport capacity for the planar channel without waterfalls (i.e., a 300 m long channel with 22 m of planar-channel relief and 0 m of waterfall relief, Figure 6b), we calculate Q_{sc} following Fernandez Luque and Van Beek (1976), and we hold Q_s/Q_{sc} constant except in Group 2. We pay particular attention to the trend in our model results (rather than the absolute magnitude) to avoid over-interpretation of the model predictions and to be consistent with the proof-of-concept level we believe the model represents.

5.3.2. Results

In Group 1, we explore varying water discharge from a 2-year to 100-year return period for the MFK reference site while holding Q_s/Q_{sc} constant across all discharges (thus, sediment flux varies with water discharge) (Figures 8a–8d). Our results show that almost all normalized erosion rates ($E_{combined}/E_{non\_wf}$, E_{wf_vert}/E_{non_wf}, E_{wf_lat}/E_{non_wf}, and E_{tl}/E_{non_wf}) increase with both increasing waterfall frequency and increasing flood magnitude (Figures 8a–8d), and that reaches with waterfalls always erode faster than waterfall-free reaches for floods of 5-year return periods or larger (i.e., $E_{combined}/E_{non\_wf}$, >1, Figure 8a). Normalized erosion rates increase with discharge because, although the erosion rates of both waterfall and non-waterfall channels ($E_{combined}$ and E_{non_wf}, respectively) increase with discharge (Figures S12a–S12e in Supporting Information S1), E_{non_wf} increases less with discharge than $E_{combined}$, due to differences in the scaling of sediment transport capacity with discharge for waterfall plunge pools versus planar channels (Scheingross & Lamb, 2021). At low discharges, waterfalls cannot effectively transport sediment out of their plunge pools, allowing the development of cover that prevents plunge pool erosion (Figure 8b, 2-year flood); however, at high discharges, the near-perpendicular impact of a waterfall jet directly into a plunge pool allows the sediment load to energetically impact the bedrock pool floor. In contrast, discharge increases in planar channels cause some sediment to be suspended, reducing the total amount of sediment impacts (Lamb et al., 2008; Scheingross et al., 2014).

In Group 1, Combined Processes Model erosion rates in waterfall-rich channels increase with waterfall frequency for two reasons. First, waterfall erosion rates are faster than that of the planar channel by total load abrasion, so increasing the fraction of channel length eroded by waterfalls (relative to erosion by total load abrasion) increases the reach-scale erosion rate. Second, individual vertical and lateral erosion rates in waterfall plunge pools increase with waterfall frequency (at discharges greater than a 2-year flood), because waterfalls are shorter with smaller pool radii. In this case, the decrease in erosion rate from decreasing drop height is outweighed by the increase in erosion rate from decreasing the plunge pool radius.

In Group 2, we vary Q_s/Q_{sc} from 0.002 to 0.5. Because Q_{sc} is calculated for the planar channel with no waterfalls (Figure 6b), a Q_s/Q_{sc} of 0.5 ensures reaching full sediment cover in reaches with waterfalls (Figure 6a) (i.e., cover will occur both in plunge pools and in planar reaches between waterfalls). While both waterfall and planar channel erosion rates increase with higher Q_s/Q_{sc}, Combined Processes Model erosion rates in waterfall-rich reaches increase modestly as compared to erosion rates in waterfall-free reaches. Therefore, at low sediment supply ($Q_s/Q_{sc} \leq 0.032$), waterfall-rich channels erode fast relative to non-waterfall channels (i.e., $E_{combined}/E_{non\_wf} > 1$) but under high sediment supply ($Q_s/Q_{sc} \geq 0.13$), waterfall-rich reaches erode slow relative to a planar reach ($E_{combined}/E_{non\_wf} < 1$). The switch from fast to slow erosion rates is partially driven by the onset of partial to full sediment cover in plunge pools, which reduces vertical and lateral erosion rates (Figures 8f and 8g) at a lower threshold Q_s/Q_{sc} than non-waterfall channels (Figures S12f–S12j in Supporting Information S1). Additionally, as sediment supply increases, the lower-slope planar reaches between waterfalls experience the onset of sediment cover before the higher-slope waterfall-free channel, causing normalized total load erosion rates to decrease and eventually drop to zero at high sediment supply ($Q_s/Q_{sc} \geq 0.1257$). Our Group 2 results show that at high sediment supply, reaches with fewer, larger waterfalls can evacuate sediment more effectively and erode more quickly than reaches with more, smaller waterfalls; however, in all cases explored in our model runs, waterfall-rich reaches at high sediment supply erode slow relative to non-waterfall channels (i.e., $E_{combined}/E_{non\_wf} < 1$ for $Q_s/Q_{sc} > 0.13$). Both of these trends are counter to the positive relationship between waterfall frequency and erosion rate found using our cosmogenic data (Figure 3), highlighting the need to collect more field data across a broader range of sediment supplies.

In Group 3, we vary median grain size from 3 mm to 20 cm. Again, dimensional erosion rates for waterfall-free and waterfall reaches both increase with grain size, but waterfall-reach erosion rates increase slower than waterfall-free rates, and then decrease precipitously at large grain sizes due to the onset of cover in the plunge-pool (Figures S12k–S12o in Supporting Information S1). Therefore, normalized reach-scale erosion rates ($E_{combined}/E_{non\_wf}$) are highest for small grain sizes and decrease with increasing grain size (Figure 8j–8m). At the largest explored grain size (D_{50} = 20 cm), sediment cover in plunge pools and planar reaches between waterfalls causes E_{wf_vert}, E_{wf_lat}, and E_{tl} to drop to zero (Figure 8j–8m and Figures S12k–S12o in Supporting Information S1); whereas for all grain sizes less than 20 cm, normalized reach-scale erosion rates increase with waterfall frequency (Figure 8j–8m).

For Groups 1–3 we vary the plunge pool radius with waterfall drop height following theory (Scheingross & Lamb, 2017) and using the best-fit relationship from our field data (Figure S8 in Supporting Information S1).

$$r_{pool} = 0.26 \times h_{wf} + 3.7 \tag{7}$$

However, in Group 4, we explore how changing the relationship between plunge pool radius and waterfall drop height influences erosion rates by multiplying Equation 7 by a constant, C, ranging from 0.67 to 3

$$r_{pool} = C[0.26 \times h_{wf} + 3.7]. \tag{8}$$

Our results show that smaller plunge-pool radii (lower C values) increase normalized waterfall and reach-scale erosion rates ($E_{combined}/E_{non\_wf}$, E_{wf_vert}/E_{non_wf}, and E_{wf_lat}/E_{non_wf}). This increase occurs because smaller pool radii create higher flow velocity in the plunge pool and concentrate sediment impacts over a smaller surface area. This increase in erosion rate is enough to offset the effect of the decreased fraction of the total channel length experiencing waterfall erosion (Figures 8n–8q). If pool radii become too large (e.g., $C = 3$), plunge-pool sediment transport capacity drops below the sediment supply and the waterfall can no longer remove sediment from the plunge pool, causing a reduction in normalized erosion rates. Given that plunge-pool radii tend to increase over time (Scheingross et al., 2017), this result indicates that if upstream waterfall retreat is halted (e.g., via retreat into a particularly resistant patch of rock), a waterfall that was initially eroding fast relative to waterfall-free reaches could become a "slow" waterfall due to the increase in plunge pool radius.

In Group 5, we test the robustness of the relationship between erosion rate and waterfall frequency by exploring different relationships between waterfall form and waterfall frequency. In Scenario 1, we use the baseline condition for the MFK reference site in which we follow the channel morphology rules used in Groups 1–4 (allowing h_{wf}, r_{pool}, h_{pool}, and S_{non_wf} to co-vary with waterfall frequency). As discussed above, in this Scenario, $E_{combined}/E_{non\_wf}$ increases with increasing waterfall frequency, due in part to increasing length of the channel eroded by waterfalls, and in part to higher vertical and lateral waterfall erosion rates caused primarily by smaller plunge-pool radii.

In Scenario 2, we allow waterfall frequency and drop height to co-vary under the same scheme as Scenario 1, but we hold plunge pool morphology constant at the median radius and depth found in our channel surveys across both MFK and Dinkey Creek ($r_{pool} = 4.5$ m, $h_{pool} = 2.5$ m). In this scenario, the erosion rate of waterfall-rich channels is fast relative to non-waterfall channels ($E_{combined}/E_{non\_wf} > 1$) and increases with waterfall frequency. However, erosion rates increase by a diminishing margin with each increase in waterfall frequency because both vertical and lateral plunge pool erosion rates decrease with decreasing drop height, as less energy is applied across the same sized plunge-pool (Figures 8s and 8t).

In Scenario 3, we hold waterfall drop height, plunge-pool radius and plunge-pool depth constants ($h_{wf} = 2.5$ m, $r_{pool} = 4.5$ m, $h_{pool} = 2.5$ m) and instead vary the slope of the planar channel between waterfalls (S_{non_wf}) to keep the total relief constant in the model reach across different waterfall frequencies. In Scenario 3, erosion rates at each waterfall are roughly constant with increasing waterfall frequency (there are slight changes in E_{wf_vert} and E_{wf_lat} due to changes in S_{non_wf}); however, normalized channel erosion rates increase with waterfall frequency.

In all three Scenarios, erosion rates in waterfall-rich reaches remained equal to or greater than erosion rates in planar reaches ($E_{combined}/E_{non\_wf} > 1$) and increased with increasing waterfall frequency (Figure 8r). We interpret this as evidence of a strong relationship between waterfall frequency and channel erosion rates, which is robust to the manner of waterfall morphology changes with waterfall frequency.

5.3.3. Model Discussion

Our model exploration shows that the presence of waterfalls can result in both fast and slow erosion relative to waterfall-free channels. Across all variables, waterfall frequency remains a dominant control on normalized erosion rates, with rates generally (but not always) increasing with increasing waterfall frequency. Our modeling results show that higher waterfall frequency results in particularly large increases in reach-scale erosion rates for reaches with low sediment supply, small grain sizes, and high-flood discharges. However, we also find that waterfalls can cause reach-scale erosion to decrease relative to waterfall-free conditions, predominantly under conditions of high sediment supply, large grain size, low flood discharge, and/or large plunge pool radius. In these

circumstances, both waterfall plunge pools and planar reaches between waterfalls may cease to erode due to the onset of sediment cover earlier than in an entirely planar channel.

Our sensitivity analysis demonstrates that waterfalls alter reach-averaged channel erosion rates under a broad range of conditions and morphology assumptions. Not only do waterfalls influence channel erosion rates under most sediment and discharge conditions, but reach-averaged erosion rates increase with waterfall frequency over a broad range of plunge pool and drop height dimensions. These model results emphasize that waterfall formation is a mechanism by which a wide variety of channels can self-adjust their morphology (in different ways) in order to erode at a rate equal to an imposed forcing.

Our model supports and provides context for other waterfall and knickzone erosion rate studies. For example, our model results agree with previous work that under a large range of conditions, waterfall-rich reaches erode fast (e.g., Crosby & Whipple, 2006; DiBiase et al., 2015; Gallen et al., 2011; Y. Hayakawa & Matsukura, 2003). Our model also indicates that waterfall erosion rates likely decrease with drainage area upstream and may become slow compared to planar-channel erosion at low drainage areas, where grain sizes are large, and flood magnitude is small (Figure 8, Figure S12 in Supporting Information S1). This result is consistent with previous work demonstrating that at small drainage areas, waterfall retreat may halt, and waterfall erosion can be negligible (Berlin & Anderson, 2007; Crosby & Whipple, 2006; DiBiase et al., 2015; Raming et al., 2024; Raming & Whipple, 2022). Furthermore, our model suggests a reason why waterfalls do not show drainage-area dependence in sediment-free experiments (e.g., Baynes, Lague, Attal, et al., 2018), by indicating that drainage-area dependence may be due to the increase in sediment size with distance upstream together with a decrease in flood magnitude.

Our model sensitivity analysis also provides insight into the channel dynamics in Dinkey Creek by supporting the idea proposed by Callahan et al. (2019) that in the Dinkey Creek landscape, channels have too little sediment to incise. Indeed, at low sediment loads and small grain sizes, both the Combined Processes Model and the total load model predict that channel erosion rates decrease almost to zero (Figure S12 in Supporting Information S1). Although waterfalls may erode faster than planar bed erosion, the channels may be unable to adjust to equilibrium because both erosion mechanisms work slowly.

6. Implications and Conclusions

Our reach-scale and basin-averaged erosion rates show that many waterfall-rich reaches erode faster than the rest of the basin. Furthermore, variability in reach-scale erosion rates can be explained primarily by waterfall frequency, with a higher frequency of waterfalls resulting in as much as a factor of 5 difference in local erosion rates for reaches with similar average-channel-slope and stream power (Figures 4, 5, and 8). These results highlight that channel slope or stream power alone may poorly predict differences in reach-scale erosion rates between waterfall-rich reaches, and instead we need to consider the combined effect of both waterfall erosion and abrasion in planar channels in order to accurately predict reach-scale erosion rates (Figures 4 and 5).

Our findings support previous numerical modeling predictions that waterfall occurrence can result in km-scale changes in river long profile morphology by altering erosion rates without greatly altering channel slopes (Rothman et al., 2023). Specifically, our cosmogenic measurements support the idea of a fast waterfall dynamic zone, by demonstrating that across a river with no high-slope knickzones and little variation in slope, channels with slightly above-average slopes and high waterfall frequencies may be eroding up to four times faster than the basin average.

While our field data show a predominance of fast waterfalls, our modeling indicates that waterfall occurrence can slow channel erosion rates under conditions of low discharge, large sediment size, large plunge pool radius, and high sediment supply. These factors suggest that waterfall erosion rates may slow as they move upstream, both in absolute terms and relative to planar-channel erosion rates, due to larger sediment size and smaller flood size. This finding is consistent with previous work demonstrating a decrease in waterfall and knickzone retreat rates moving upstream (e.g., Berlin & Anderson, 2007; Crosby & Whipple, 2006; DiBiase et al., 2015; Raming & Whipple, 2022).

If fast waterfall erosion is most likely to occur under low sediment supply and with small grain sizes, we hypothesize that fast-waterfall rich channels could also alter rivers in terms of channel planform and lateral migration. Fast-eroding waterfall reaches likely coincide with low lateral erosion rates due to the lack of sediment

cover and bed roughness needed to drive high rates of lateral sediment impacts (Baynes et al., 2020; Turowski, 2018). This conjecture agrees with our field observations and previous findings that waterfall-rich channels tend to be narrow, with lateral erosion mostly confined to plunge pools (e.g., Baynes et al., 2022; DiBiase et al., 2015). Furthermore, if waterfalls deflect grain impacts equally toward all plunge-pool walls (Scheingross et al., 2017) rather than preferentially toward the cutbank channel wall as in sinuous channels (Turowski, 2018), waterfalls may also alter channel planform evolution by slowing bedrock channel migration. In sum, our field and modeling results highlight waterfalls as important channel features that can both drive reach-scale erosion rates and shape river morphology, and potentially watershed morphology over larger spatial scales.

Data Availability Statement

All cosmogenic nuclide data are available in Tables S1–S4 and S7, and all survey and pebble count data are available in Tables S5–S9 in Supporting Information S2 as well as in a Zenodo data set repository (Rothman, 2024b). We have also supplied codes for identifying channel width using TopoToolbox 2 (Schwanghart & Scherler, 2014), and for running the Combined Processes Model (including codes for calculating waterfall erosion previously made available in the supporting information of Scheingross and Lamb (2016) and Total Load Erosion code written by Michael P. Lamb and edited by Joel S. Scheingross as per Lamb et al. (2008)) available in a Zenodo software repository (Rothman, 2024a). All codes were written in MATLAB (2022).

Acknowledgments

We acknowledge funding from NSF (EAR-1946342 to JSS and SWM), and National Center for Airborne Laser Mapping (NCALM) lidar collection via a seed grant to SDR. Paul Hardwick and Joshua Flickinger at the U.S. Forest Service and Gabriel Venegas at the National Park Service facilitated access to pre-existing lidar, and Danielle Shaffer at Sequoia and Kings Canyon National Parks assisted with sample collection permitting. We thank Darrin McQuoid for maintaining the Dinkey Creek access trail and documenting waterfall-rich rivers in the Sierra Nevada, Julien Charreau and Simon Mudd for helping us use Basinga, and LSD Topotools, Erika Groh, Michael Robinson and Laura Wade for field assistance, and Jack Tarricone for assisting with snow water equivalent modeling. This paper benefited from constructive review by Paul Carling, two anonymous reviewers and an anonymous Associate Editor.

References

Balco, G., Stone, J. O., Lifton, N. A., & Dunai, T. J. (2008). A complete and easily accessible means of calculating surface exposure ages or erosion rates from ^{10}Be and ^{26}Al measurements. *Quaternary Geochronology*, *3*(3), 174–195. https://doi.org/10.1016/j.quageo.2007.12.001

Bateman, P. C., & Jones, D. R. (1972). *Geologic map of the Huntington Lake quadrangle, central Sierra Nevada, California [Map]*. USGS.

Baynes, E. R. C., Attal, M., Niedermann, S., Kirstein, L. A., Dugmore, A. J., & Naylor, M. (2015). Erosion during extreme flood events dominates Holocene canyon evolution in northeast Iceland. *Proceedings of the National Academy of Sciences*, *112*(8), 2355–2360. https://doi.org/10.1073/pnas.1415443112

Baynes, E. R. C., Lague, D., Attal, M., Gangloff, A., Kirstein, L. A., & Dugmore, A. J. (2018a). River self-organisation inhibits discharge control on waterfall migration. *Scientific Reports*, *8*(1), 2444. https://doi.org/10.1038/s41598-018-20767-6

Baynes, E. R. C., Lague, D., & Kermarrec, J.-J. (2018b). Supercritical river terraces generated by hydraulic and geomorphic interactions. *Geology*, *46*(6), 499–502. https://doi.org/10.1130/G40071.1

Baynes, E. R. C., Lague, D., Steer, P., Bonnet, S., & Illien, L. (2020). Sediment flux-driven channel geometry adjustment of bedrock and mixed gravel–bedrock rivers. *Earth Surface Processes and Landforms*, *45*(14), 3714–3731. https://doi.org/10.1002/esp.4996

Baynes, E. R. C., Lague, D., Steer, P., & Davy, P. (2022). Dynamic bedrock channel width during knickpoint retreat enhances undercutting of coupled hillslopes. *Earth Surface Processes and Landforms*, *47*(15), 3629–3640. https://doi.org/10.1002/esp.5477

Beer, A. R., & Turowski, J. M. (2015). Bedload transport controls bedrock erosion under sediment-starved conditions. *Earth Surface Dynamics*, *3*(3), 291–309. https://doi.org/10.5194/esurf-3-291-2015

Beeson, H. W., & McCoy, S. W. (2019). Geomorphic signatures of the transient fluvial response to tilting. *Earth Surface Dynamics Discussions*, 1–39. https://doi.org/10.5194/esurf-2019-24

Beeson, H. W., & McCoy, S. W. (2022). Disequilibrium river networks dissecting the western slope of the Sierra Nevada, California, USA, record significant late Cenozoic tilting and associated surface uplift. *GSA Bulletin*, *134*(11–12), 2809–2853. https://doi.org/10.1130/B35463.1

Berlin, M. M., & Anderson, R. S. (2007). Modeling of knickpoint retreat on the Roan Plateau, western Colorado. *Journal of Geophysical Research*, *112*(F3), F03S06. https://doi.org/10.1029/2006JF000553

Brocard, G. Y., Willenbring, J. K., Miller, T. E., & Scatena, F. N. (2016). Relict landscape resistance to dissection by upstream migrating knickpoints. *Journal of Geophysical Research: Earth Surface*, *121*(6), 1182–1203. https://doi.org/10.1002/2015JF003678

Callahan, R. P., Ferrier, K. L., Dixon, J., Dosseto, A., Hahm, W. J., Jessup, B. S., et al. (2019). Arrested development: Erosional equilibrium in the southern Sierra Nevada, California, maintained by feedbacks between channel incision and hillslope sediment production. *GSA Bulletin*, *131*(7–8), 1179–1202. https://doi.org/10.1130/B35006.1

Chatanantavet, P., & Parker, G. (2009). Physically based modeling of bedrock incision by abrasion, plucking, and macroabrasion. *Journal of Geophysical Research*, *114*(F4), F04018. https://doi.org/10.1029/2008JF001044

Chilton, K. D., & Spotila, J. A. (2022). Uncovering the controls on Fluvial Bedrock Erodibility and Knickpoint expression: A high-resolution comparison of bedrock properties between knickpoints and non-knickpoint reaches. *Journal of Geophysical Research: Earth Surface*, *127*(3), e2021JF006511. https://doi.org/10.1029/2021JF006511

Crosby, B. T., & Whipple, K. X. (2006). Knickpoint initiation and distribution within fluvial networks: 236 waterfalls in the Waipaoa River, North Island, New Zealand. *Geomorphology*, *82*(1–2), 16–38. https://doi.org/10.1016/j.geomorph.2005.08.023

DiBiase, R. A., & Whipple, K. X. (2011). The influence of erosion thresholds and runoff variability on the relationships among topography, climate, and erosion rate. *Journal of Geophysical Research*, *116*(F4), F04036. https://doi.org/10.1029/2011JF002095

DiBiase, R. A., Whipple, K. X., Lamb, M. P., & Heimsath, A. M. (2015). The role of waterfalls and knickzones in controlling the style and pace of landscape adjustment in the western San Gabriel Mountains, California. *Geological Society of America Bulletin*, *127*(3–4), 539–559. https://doi.org/10.1130/B31113.1

Duvall, A., Kirby, E., & Burbank, D. (2004). Tectonic and lithologic controls on bedrock channel profiles and processes in coastal California. *Journal of Geophysical Research*, *109*(F3), F03002. https://doi.org/10.1029/2003JF000086

Ferguson, R. (2007). Flow resistance equations for gravel- and boulder-bed streams. *Water Resources Research*, *43*(5), 2006WR005422. https://doi.org/10.1029/2006WR005422

Fernandez Luque, R., & Van Beek, R. (1976). Erosion and transport of bed-load sediment. *Journal of Hydraulic Research*, *14*(2), 127–144. https://doi.org/10.1080/00221687609499677

Finnegan, N. J., Hallet, B., Montgomery, D. R., Zeitler, P. K., Stone, J. O., Anders, A. M., & Yuping, L. (2008). Coupling of rock uplift and river incision in the Namche Barwa-Gyala Peri massif, Tibet. *Geological Society of America Bulletin*, *120*(1–2), 142–155. https://doi.org/10.1130/B26224.1

Frankel, K. L., Pazzaglia, F. J., & Vaughn, J. D. (2007). Knickpoint evolution in a vertically bedded substrate, upstream-dipping terraces, and Atlantic slope bedrock channels. *Geological Society of America Bulletin*, *119*(3–4), 476–486. https://doi.org/10.1130/B25965.1

Gallen, S. F., Wegmann, K. W., Frankel, K. L., Hughes, S., Lewis, R. Q., Lyons, N., et al. (2011). Hillslope response to knickpoint migration in the Southern Appalachians: Implications for the evolution of post-orogenic landscapes. *Earth Surface Processes and Landforms*, *36*(9), 1254–1267. https://doi.org/10.1002/esp.2150

Gilbert, G. K. (1890). *The history of the Niagara River*. Lyon.

Gilbert, G. K. (1907). Rate of recession of Niagara Falls. *The Journal of Geology*, *15*(6).

Gillespie, A. R., & Clark, D. H. (2011). Glaciations of the Sierra Nevada, California, USA. In *Developments in quaternary sciences* (Vol. 15, pp. 447–462). Elsevier. https://doi.org/10.1016/B978-0-444-53447-7.00034-9

Groh, E. L., & Scheingross, J. S. (2022). Morphologic signatures of autogenic waterfalls: A case study in the San Gabriel Mountains, California. *Geology*, *50*(2), 248–253. https://doi.org/10.1130/G49320.1

Haviv, I., Enzel, Y., Whipple, K. X., Zilberman, E., Matmon, A., Stone, J., & Fifield, K. L. (2010). Evolution of vertical knickpoints (waterfalls) with resistant caprock: Insights from numerical modeling. *Journal of Geophysical Research*, *115*(F3), F03028. https://doi.org/10.1029/2008JF001187

Haviv, I., Enzel, Y., Whipple, K. X., Zilberman, E., Stone, J., Matmon, A., & Fifield, L. K. (2006). Amplified erosion above waterfalls and oversteepened bedrock reaches. *Journal of Geophysical Research*, *111*(F4), F04004. https://doi.org/10.1029/2006JF000461

Hayakawa, Y., & Matsukura, Y. (2003). Recession rates of waterfalls in Boso Peninsula, Japan, and a predictive equation. *Earth Surface Processes and Landforms*, *28*(6), 675–684. https://doi.org/10.1002/esp.519

Hayakawa, Y. S., & Matsukura, Y. (2010). Stability analysis of waterfall cliff face at Niagara Falls: An implication to erosional mechanism of waterfall. *Engineering Geology*, *116*(1–2), 178–183. https://doi.org/10.1016/j.enggeo.2010.08.004

Holland, W. N., & Pickup, G. (1976). Flume study of knickpoint development in stratified sediment. *Geological Society of America Bulletin*, *87*(1), 76. https://doi.org/10.1130/0016-7606(1976)87<76:FSOKDI>2.0.CO;2

Howard, A. D., Dietrich, W. E., & Seidl, M. A. (1994). Modeling fluvial erosion on regional to continental scales. *Journal of Geophysical Research*, *99*(B7), 13971–13986. https://doi.org/10.1029/94JB00744

Inoue, T., Scheingross, J. S., Hiramatsu, Y., Tanigawa, S., & Sumner, T. (2023). Waterfall height sets the mechanism and rate of upstream retreat. *Geology*, *51*(7), 693–697. https://doi.org/10.1130/G51039.1

Izumi, N., Yokokawa, M., & Parker, G. (2017). Incisional cyclic steps of permanent form in mixed bedrock-alluvial rivers. *Journal of Geophysical Research: Earth Surface*, *122*(1), 130–152. https://doi.org/10.1002/2016JF003847

Jansen, J. D., Fabel, D., Bishop, P., Xu, S., Schnabel, C., & Codilean, A. T. (2011). Does decreasing paraglacial sediment supply slow knickpoint retreat? *Geology*, *39*(6), 543–546. https://doi.org/10.1130/G32018.1

Lague, D. (2014). The stream power river incision model: Evidence, theory and beyond. *Earth Surface Processes and Landforms*, *39*(1), 38–61. https://doi.org/10.1002/esp.3462

Lague, D., Hovius, N., & Davy, P. (2005). Discharge, discharge variability, and the bedrock channel profile: Discharge variability and channel profile. *Journal of Geophysical Research*, *110*(F4), F04006. https://doi.org/10.1029/2004JF000259

Lamb, M. P., & Dietrich, W. E. (2009). The persistence of waterfalls in fractured rock. *GSA Bulletin*, *121*(7–8), 1123–1134. https://doi.org/10.1130/B26482.1

Lamb, M. P., Dietrich, W. E., & Sklar, L. S. (2008). A model for fluvial bedrock incision by impacting suspended and bed load sediment. *Journal of Geophysical Research*, *113*(F3), F03025. https://doi.org/10.1029/2007JF000915

Lamb, M. P., Howard, A. D., Dietrich, W. E., & Perron, J. T. (2007). Formation of amphitheater-headed valleys by waterfall erosion after large-scale slumping on Hawai'i. *Geological Society of America Bulletin*, *119*(7–8), 805–822. https://doi.org/10.1130/B25986.1

Lifton, N., Sato, T., & Dunai, T. J. (2014). Scaling in situ cosmogenic nuclide production rates using analytical approximations to atmospheric cosmic-ray fluxes. *Earth and Planetary Science Letters*, *386*, 149–160. https://doi.org/10.1016/j.epsl.2013.10.052

Lukens, C. E., Riebe, C. S., Sklar, L. S., & Shuster, D. L. (2016). Grain size bias in cosmogenic nuclide studies of stream sediment in steep terrain. *Journal of Geophysical Research: Earth Surface*, *121*(5), 978–999. https://doi.org/10.1002/2016JF003859

Mackey, B. H., Scheingross, J. S., Lamb, M. P., & Farley, K. A. (2014). Knickpoint formation, rapid propagation, and landscape response following coastal cliff retreat at the last interglacial sea-level highstand: Kaua'i, Hawai'i. *Geological Society of America Bulletin*, *126*(7–8), 925–942. https://doi.org/10.1130/B30930.1

Malatesta, L. C., & Lamb, M. P. (2018). Formation of waterfalls by intermittent burial of active faults. *GSA Bulletin*, *130*(3–4), 522–536. https://doi.org/10.1130/B31743.1

MATLAB. (2022). Version 9.13 (R2022b). Natick, Massachusetts: The MathWorks Inc.

Matthews, R. A., & Burnett, J. L. (1965). *Geologic map of California: Fresno sheet [Map]*. California Division of Mines and Geology.

Moore, J. G., & Sisson, T. W. (1987). *Preliminary geologic map of Sequoia and Kings Canyon National Parks, California [Map]*. USGS. Retrieved from https://pubs.usgs.gov/publication/ofr87651

Mudd, S. M., Clubb, F. J., Grieve, S. W. D., Milodowski, D. T., Gailleton, B., Hurst, M. D., et al. (2023). *LSDtopotools/LSDTopoTools2: LSDTopoTools2 v0.9 (version 0.9)*. [Zenodo]. https://doi.org/10.5281/zenodo.8076231

Mudd, S. M., Harel, M.-A., Hurst, M. D., Grieve, S. W. D., & Marrero, S. M. (2016). The CAIRN method: Automated, reproducible calculation of catchment-averaged denudation rates from cosmogenic nuclide concentrations. *Earth Surface Dynamics*, *4*(3), 655–674. https://doi.org/10.5194/esurf-4-655-2016

Perron, J. T., & Royden, L. (2013). An integral approach to bedrock river profile analysis. *Earth Surface Processes and Landforms*, *38*(6), 570–576. https://doi.org/10.1002/esp.3302

Prism Climate Group, Oregon State University. (2024). [Dataset]. Retrieved from https://prism.oregonstate.edu

Raming, L. W., & Whipple, K. X. (2022). When knickzones limit upstream transmission of base-level fall: An example from Kaua'i, Hawai'i. *Geology*, *50*(12), 1382–1386. https://doi.org/10.1130/G50019.1

Raming, L. W., Whipple, K. X., & Strauch, A. M. (2024). Limits to knickzone retreat and bedrock river incision on the Hawaiian Islands. *Earth Surface Processes and Landforms*, *49*(6), 1914–1931. https://doi.org/10.1002/esp.5806

Roda-Boluda, D. C., D'Arcy, M., Whittaker, A. C., Gheorghiu, D. M., & Rodés, Á. (2019). 10Be erosion rates controlled by transient response to normal faulting through incision and landsliding. *Earth and Planetary Science Letters*, *507*, 140–153. https://doi.org/10.1016/j.epsl.2018.11.032

Rothman, S. D. (2024a). SophieRothman/waterfall_erosion_rates: Removed tables (Version v4) [Computer software]. *Zenodo*. https://doi.org/10.5281/zenodo.13835638

Rothman, S. D. (2024b). Waterfall reach and basin morphology, and pebble counts (Version v1) [Dataset]. *Zenodo*. https://doi.org/10.5281/zenodo.13835511

Rothman, S. D., Scheingross, J. S., McCoy, S. W., & Dow, H. W. (2023). Impacts of spontaneous waterfall development on bedrock river longitudinal profile morphology. *Journal of Geophysical Research: Earth Surface*, *128*(7), e2022JF007057. https://doi.org/10.1029/2022JF007057

Rouse, H. (1936). Discharge characteristics of the free overfall. *Civil Engineering*, *6*(4), 257–260.

Rouse, H. (1937). Pressure distribution and acceleration at the free overfall. *Civil Engineering*, *7*, 518.

Scheingross, J. S., Brun, F., Lo, D. Y., Omerdin, K., & Lamb, M. P. (2014). Experimental evidence for fluvial bedrock incision by suspended and bedload sediment. *Geology*, *42*(6), 523–526. https://doi.org/10.1130/G35432.1

Scheingross, J. S., & Lamb, M. P. (2016). Sediment transport through self-adjusting, bedrock-walled waterfall plunge pools. *Journal of Geophysical Research: Earth Surface*, *121*(5), 939–963. https://doi.org/10.1002/2015JF003620

Scheingross, J. S., & Lamb, M. P. (2017). A mechanistic model of waterfall plunge pool erosion into bedrock. *Journal of Geophysical Research: Earth Surface*, *122*(11), 2079–2104. https://doi.org/10.1002/2017JF004195

Scheingross, J. S., & Lamb, M. P. (2021). Mass balance controls on sediment scour and bedrock erosion in waterfall plunge pools. *Geology*, *49*(9), 1084–1088. https://doi.org/10.1130/G48881.1

Scheingross, J. S., Lamb, M. P., & Fuller, B. M. (2019). Self-formed bedrock waterfalls. *Nature*, *567*(7747), 229–233. https://doi.org/10.1038/s41586-019-0991-z

Scheingross, J. S., Limaye, A. B., McCoy, S. W., & Whittaker, A. C. (2020). The shaping of erosional landscapes by internal dynamics. *Nature Reviews Earth & Environment*, *1*(12), 661–676. https://doi.org/10.1038/s43017-020-0096-0

Scheingross, J. S., Lo, D. Y., & Lamb, M. P. (2017). Self-formed waterfall plunge pools in homogeneous rock. *Geophysical Research Letters*, *44*(1), 200–208. https://doi.org/10.1002/2016GL071730

Schwanghart, W., & Kuhn, N. J. (2010). TopoToolbox: A set of Matlab functions for topographic analysis. *Environmental Modelling & Software*, *25*(6), 770–781. https://doi.org/10.1016/j.envsoft.2009.12.002

Schwanghart, W., & Scherler, D. (2014). Short communication: TopoToolbox 2 – MATLAB-based software for topographic analysis and modeling in Earth surface sciences. *Earth Surface Dynamics*, *2*(1), 1–7. https://doi.org/10.5194/esurf-2-1-2014

Sisson, T. W., & Moore, J. G. (2013). *Geologic map of southwestern Sequoia National Park, Tulare County, California [Map]*. USGS. Retrieved from https://pubs.usgs.gov/of/2013/1096/

Sklar, L. S., & Dietrich, W. E. (2001). Sediment and rock strength controls on river incision into bedrock. *Geology*, *29*(12), 1087. https://doi.org/10.1130/0091-7613(2001)029<1087:SARSCO>2.0.CO;2

Sklar, L. S., & Dietrich, W. E. (2004). A mechanistic model for river incision into bedrock by saltating bed load. *Water Resources Research*, *40*(6), W06301. https://doi.org/10.1029/2003WR002496

Stock, G. M., Anderson, R. S., & Finkel, R. C. (2005). Rates of erosion and topographic evolution of the Sierra Nevada, California, inferred from cosmogenic ^{26}Al and ^{10}Be concentrations. *Earth Surface Processes and Landforms*, *30*(8), 985–1006. https://doi.org/10.1002/esp.1258

Stokes, M. F., Larsen, I. J., Goldberg, S. L., McCoy, S. W., Prince, P. P., & Perron, J. T. (2023). The erosional signature of drainage divide motion along the blue ridge escarpment. *Journal of Geophysical Research: Earth Surface*, *128*(1), e2022JF006757. https://doi.org/10.1029/2022JF006757

Turowski, J. M. (2018). Alluvial cover controlling the width, slope and sinuosity of bedrock channels. *Earth Surface Dynamics*, *6*(1), 29–48. https://doi.org/10.5194/esurf-6-29-2018

Turowski, J. M., Badoux, A., Leuzinger, J., & Hegglin, R. (2013). Large floods, alluvial overprint, and bedrock erosion. *Earth Surface Processes and Landforms*, *38*(9), 947–958. https://doi.org/10.1002/esp.3341

Valla, P. G., van der Beek, P. A., & Carcaillet, J. (2010). Dating bedrock gorge incision in the French Western Alps (Ecrins-Pelvoux massif) using cosmogenic ^{10}Be. *Terra Nova*, *22*(1), 18–25. https://doi.org/10.1111/j.1365-3121.2009.00911.x

Wakabayashi, J. (2013). Paleochannels, stream incision, erosion, topographic evolution, and alternative explanations of paleoaltimetry, Sierra Nevada, California. *Geosphere*, *9*(2), 191–215. https://doi.org/10.1130/GES00814.1

Whittaker, A. C., & Boulton, S. J. (2012). Tectonic and climatic controls on knickpoint retreat rates and landscape response times. *Journal of Geophysical Research*, *117*(F2), 2011JF002157. https://doi.org/10.1029/2011JF002157

Yanites, B. J., Tucker, G. E., Mueller, K. J., & Chen, Y.-G. (2010). How rivers react to large earthquakes: Evidence from central Taiwan. *Geology*, *38*(7), 639–642. https://doi.org/10.1130/G30883.1

Zhang, L., Parker, G., Stark, C. P., Inoue, T., Viparelli, E., Fu, X., & Izumi, N. (2015). Macro-roughness model of bedrock–alluvial river morphodynamics. *Earth Surface Dynamics*, *3*(1), 113–138. https://doi.org/10.5194/esurf-3-113-2015

Erratum

The originally published version of this article contained typographical errors. In Figure 2, panels f and j should be renamed as “DNK-03” and “DNK-06,” respectively. The errors have been corrected, and this may be considered the authoritative version of record.